ENERGY HARVESTER APPLICATION OF LARGE-DEFORMATION-PIEZOELECTRICS WITH SYNCHRONIZED-MECHANICAL-SWITCH CIRCUIT

by

Qiaoyi Wei

Bachelor of Engineering, Beijing University of Technology, 2015

Submitted to the Graduate Faculty of

Swanson School of Engineering in partial fulfillment

of the requirements for the degree of

Master of Science

University of Pittsburgh

2017

UNIVERSITY OF PITTSBURGH

SWANSON SCHOOL OF ENGINEERING

This thesis was presented

by

Qiaoyi Wei

It was defended on

April 25, 2017

and approved by

William (Buddy) Clark, PhD, Professor, Department of Mechanical Engineering and Materials Science

Jung-Kun Lee, PhD, Associate Professor, Department of Mechanical Engineering and Materials Science

Geoffrey Hutchison, PhD, Associate Professor, Department of Chemistry

Thesis Advisor: William (Buddy) Clark, PhD, Professor, Department of Mechanical Engineering and Materials Science

ENERGY HARVESTER APPLICATION OF LARGE-DEFORMATION-PIEZOELECTRICS WITH SYNCHRONIZED-MECHANICAL-SWITCH CIRCUIT

Qiaoyi Wei, M.S.

University of Pittsburgh, 2017

Growing demand for battery-free or self-powered designs of electronics encourages the development of energy harvesting from mechanical vibrations or impacts using piezoelectric materials. Piezoelectric materials used to date are characterized by high elastic moduli and high resonant frequency (kHz range), and therefore their performances are diminished at low frequencies (0.1~100 Hz), which are, however, the frequencies of the majority of mechanical energy sources in the environment.

This thesis reviews the techniques and interface circuits that have been developed to improve the power outputs of piezoelectric energy harvesters for low frequency applications. Inspired by the Synchronized-Switch Harvester (SSH) circuit, this thesis introduces a concept of Synchronized-Mechanical-Switch Harvester (SMSH) by taking advantage of large-deformation piezoelectric materials and structures to overcome the current issues of SSH, which includes the requirement of external power supply and displacement sensor. Thus, current piezoelectric materials and their mechanisms of improving piezo-property are also reviewed. One novel material with low elastic modulus, a piezoelectric foam, and one low-stiffness piezoelectric structure, a THUNDER device, are selected as candidates for evaluation of SMSH.

For the device tested, up to 55% increase of output power was obtained by SMSH compared to traditional Full-Wave Rectifier (FWR) interface circuit in the frequency range of 4Hz to 65Hz. The influential factors of output power of SMSH are studied and discussed.

TABLE OF CONTENTS

LIST OF TABLES

LIST OF FIGURES

PREFACE

I would first like to thank my thesis advisor Professor William Clark of Department of Mechanical Engineering and Material Science. His encouragement always motivates me to solve whatever trouble we encountered. I really appreciate his patience when discussing the research problems. The optimism I learn from him is my life-time treasure.

I would also like to acknowledge Professor Geoffrey Hutchison of Department of Chemistry. Without the help from him and his research group, the experiment part of the project would not be able to be completed. I also would like to say thank you to the Civil Environment Lab group who were so generous to share some chemical equipment with us.

Finally, I must express my very profound gratitude to my parents and to my boyfriend for providing me with unfailing support throughout my years of study and through the process of researching and writing this thesis. I would also like to thank my lab mates and friends. You make me enjoy working and living every day. This accomplishment would not have been possible without you. Thank you.

Author,

Qiaoyi Wei

1.0 INTRODUCTION

1.1 MOTIVATION FOR THE STUDY

1.1.1 Study of energy harvesting and interface circuits

The miniaturization of electronic devices precipitates the development of low-power-consuming electronic devices, such as wearable devices, implanted devices, mobile electronics and wireless network nodes. Due to the high cost of replacing or manually charging batteries or the fact that many batteries are embedded in devices and not serviceable configuration, there is a growing demand for battery-free or self-powered designs of electronics. Compared to other self-power systems, for instance the solar cell, kinetic energy harvesters stand out for their advantages of stability, ability to be miniaturized and for the adjustability of their mechanical and piezoelectric properties.

Power output of piezoelectric power scavengers is characterized by relatively high voltage but low current owing to the very large internal impedance based on the insulator nature of the piezoelectrics. The low profile of power output from the piezoelectric energy harvester provides itself a good match for self-powered low-power-consuming electronic devices. An example self-power process using piezoelectric energy conversion is present in Figure 1. Three parts are included in the system to achieve the energy transformation: 1) piezoelectric element

that is excited by environment and that outputs electricity; 2) interface circuit for rectifying the AC electricity output from the first part, which is designed to extract maximum power from the piezoelectric element and 3) energy storage part.

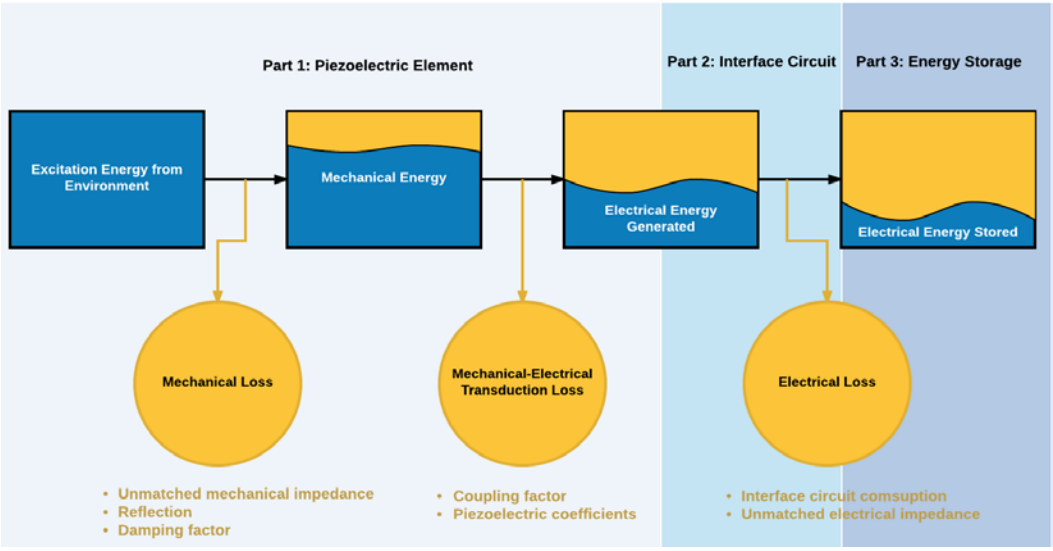

Figure 1. Schematic of energy conversion process of energy harvester system and energy loss related parameters (Kim et al. 2012).

Each of the segments in Figure 1 exhibit energy losses (Kim et al. 2012). There is mechanical energy loss as the piezoelectric element is subject to excitation from the environment due to unmatched mechanical impedance, reflection of energy on the surface, and damping etc. Since the electro-mechanical coupling quality can never be perfect in a piezoelectric element, only a fraction of the input mechanical energy can be transferred into electrical energy. Finally, this energy is then delivered to energy storage element through the interface circuit with electrical loss because of the power consumption of the circuit and the unmatched electrical impedance.

This thesis is motivated by optimization of the energy harvester system by reducing the energy loss through: exploring piezoelectric element with high mechanical compatibility as well as excellent piezoelectric response; and reducing the power consumption from interface circuit in order to maximize the output power from the energy harvester.

1.1.2 Study of piezoelectric materials

Since J. and P. Curie discovered piezoelectricity, people have never stopped exploring the possibilities of piezoelectric materials, which have been used in critical applications across military and industrial fields. Three milestones in the development of piezoelectric materials can be identified: In the World War I, Paul Langevin firstly tried to apply crystal quartz as an ultrasonic transducer to locate German submarines; The discovery of ferroelectricity in Rochelle salt ($KNaC_4H_4O_6$; Seignettesalz in German language) and barium oxide-titanium oxide compositions ($BaTiO_3$) set off a remarkable development in polycrystalline ceramic materials between 1941 and 1947; A few years later, Jaffe et al (Jaffe et al. 1954) found lead zicronate titanate (PZT) to be a strong and stable piezoelectric material whose compositions have constituted dominant piezo-ceramics studies even in present days.

PZT as a featured piezoelectric ceramic has realized widespread application in various field, especially in MEMS (micro-electro-mechanical systems), in forms such as ultrasonic transducers, sensors, actuators and energy harvesters. In spite of the success of PZT, many applications have design and operating requirements that PZT cannot satisfy, which has encouraged the continual investigation of piezoelectric polymers and other polymer-ceramic compositions as outlined in Table 1.

Of particular interest in this thesis is piezoelectric polymer materials, such as PVDF, P(VDF-TrFE), and polymer foam. For some applications, piezoelectric polymers have a significant advantage in mechanical properties compared to ceramics, given their flexibility or mechanical compatibility with certain inputs. For example, in human interfaces, such as harvesting energy of human motions, the movements tend to be low force, low frequency, and high range, all of which are better suited to polymers than ceramics. Piezoelectric polymers can have processing advantages too, as they can be used to fabricate piezo-MEMS at lower temperature and at less cost than their inorganic counterparts.

Table 1. Piezoelectric parameters for piezoelectric materials (Harrison & Ounaies 2001; Polla & Francis 1998)

Material	**Formula**	**Form**	**Piezoelectric Constant (pC/N or pm/V)**	**Maximum Used Temperature** (℃)
PVDF	$(CH_2CF_2)_n$	Oriented polymer	$d_{31} = 28$	80
P(VDF-TrFE) 75/25 mol%	$(CH_2CF_2)_a(CH_2CHF)_b$	Oriented polymer	$d_{33} = -38$	95
Nylon-11	$(NH\text{-}(CH_2)_{10}CO)_n$	Crystallized polymer	$d_{31} = 14$ @107℃	185
PZT	$PbZr_{0.6}Ti_{0.4}O_3$	Polycrystalline ceramic	$d_{33} = 117$	217
PLZT	$Pb_{0.925}La_{0.5}Zr_{0.56}Ti_{0.44}O_3$	Polycrystalline ceramic	$d_{33} = 545$	328
Barium titanate	$BaTiO_3$	Single Crystal	$d_{15} = 587$	115
PZT-PVDF	-	Ceramic-Polymer composite	$d_{33} = 30 \sim 89$	100

The essential factor that limits the development of piezoelectric polymers is that the piezoelectric response of polymers is weak compared with that of the inorganics. The large

disparity of piezoelectric coefficients for current commonly used piezoelectric polymer and ceramics is shown in Table 1(Harrison & Ounaies 2001; Polla & Francis 1998).

A tradeoff solution is to create ceramic-polymer composites, combining the high piezoelectric coefficients of inorganics and the excellent mechanical properties of polymer. The advantages of these two components are complementary in composites. However, new issues, for instance stability, are introduced into composite materials.

Choosing the piezoelectric material that fits the application is an essential step for studying energy harvesters. This thesis is primarily focused on low-modulus piezo-materials and low-stiffness piezoelectric structure that are with suitable for SMSH applications.

1.2 THESIS ORGANIZATION

Studies about piezoelectric-based materials and devices are inherently inter-disciplinary. The physical foundation of piezoelectricity is elaborated in Chapter 2. The definitions of relevant parameters are explained, which lead to the description of piezoelectric performance governing equations, in terms of electrical fields, electric displacement in the material, stress applied, and strain produced.

Chapter 3 provides background information about common configurations of energy scavengers, and different interface circuits in the harvester systems. Here, Full-Wave Rectifier (FWR), voltage doubler and Synchronized-Switch Harvester (SSH) circuits are introduced and compared. Based on the theory of SSH, this thesis puts forward a new design for a rectifier circuit, of which the switch control part is substituted with a mechanical switch formed by the electrodes attached on the extremely flexible piezoelectric material and two parallel metal plates,

to reduce the power consumption from the switch control circuit. The details of the Synchronized-Mechanical-Switch Harvester (SMSH) is described in Chapter 4.

To explore materials that are ideally suited for the SMSH method, including large-deformation capability and high piezoelectric response, the nature of piezoelectricity in different piezo-materials is investigated in Chapter 5. Ceramics, polymers and ceramic-polymer composites as three typical piezoelectric material types are studied. A doped polyurethane foam and the PZT thin film with THUNDER configuration are found to be excellent candidates for the application. The former polymer foam shows promising property in both mechanical and piezoelectric aspects. This foam has been developed by a cooperative research group using a non-traditional method which will be introduced in section 5.4.

After choosing the material, experiments are designed to prove the feasibility of the SMSH. Chapter 6 describes the synthesis detail of the polymer foam, as well as the establishment of measurement unit for piezoelectric coefficients. Additionally, the construction of SMSH and the test rig for evaluating the performance are also described in Chapter 6. The results of experiments are analyzed in Chapter 7.

2.0 PIEZOELECTRICITY

2.1 DEFINITION OF PIEZOELECTRICITY

A property whereby a material develops a dielectric displacement (or polarization) in response to an applied force, and, reversely, develops a strain in response to an applied electric field, is known as piezoelectricity. The former phenomenon is known as the direct piezoelectric effect and the latter one is indirect piezoelectric effect. The induced charge per unit area linearly depends on the applied stress. Based on this property, piezoelectric materials are able to convert mechanical energy to electricity, which enables promising application in generators, actuators, sensors and transducers.

2.2 MATERIAL COEFFICIENTS

The nature of piezoelectricity is the coupling of mechanical process and electrical operation. Understanding the coefficients relevant to mechanical and electrical properties as well as the coupling of both processes are the prerequisites for further study of piezoelectricity in the materials. In this section, the essential coefficients are introduced.

2.2.1 Elastic coefficient

The elastic stiffness constant *c* and elastic compliance constant *s* of the material are given by the Hooke's Law:

$$T_i = c_{ij} S_j \tag{2-1}$$

$$S_j = s_{ji} T_i \tag{2-2}$$

where *T* is the applied stress and *S* is the strain of the material. The unit of *c* and *s* are thus (N/m^2) and (m^2/N) respectively. The subscripts *i,j* of each constant indicate the direction of that element considering the anisotropic nature of the material. The subscripts of the constants in the above equation are commonly simplified (Nye 1985), as the elements of tensor are contracted to numbers that span 1 to 6, where 1, 2, 3 designating the directions of normal stress and 4, 5, 6 represent the shear stress directions (Figure 2). The replacement rule is shown in matrix below:

$$\begin{bmatrix} T_{11} & T_{12} & T_{13} \\ T_{21} & T_{22} & T_{23} \\ T_{31} & T_{32} & T_{33} \end{bmatrix} = \begin{bmatrix} T_1 & T_6 & T_5 \\ T_6 & T_2 & T_4 \\ T_5 & T_4 & T_3 \end{bmatrix}, \begin{bmatrix} S_{11} & S_{12} & S_{13} \\ S_{21} & S_{22} & S_{23} \\ S_{31} & S_{32} & S_{33} \end{bmatrix} = \begin{bmatrix} S_1 & S_6/2 & S_5/2 \\ S_6/2 & S_2 & S_4/2 \\ S_5/2 & S_4/2 & T_3 \end{bmatrix} \tag{2-3}$$

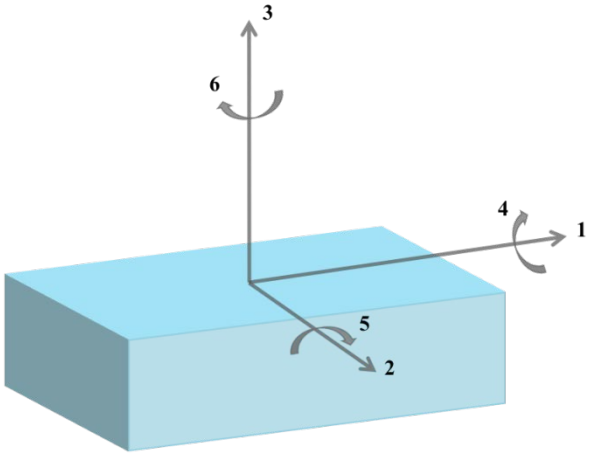

Figure 2. Illustration of reduced form of tensor direction

2.2.2 Dielectric coefficient

The dielectric constant is aimed to quantify the extent of response of dipoles within the piezoelectric material due to the presence of electric field, thereby providing the ability of a material to store the electricity in an electric field. Most insulator materials, in addition to piezoelectric materials, exhibit the dielectric property.

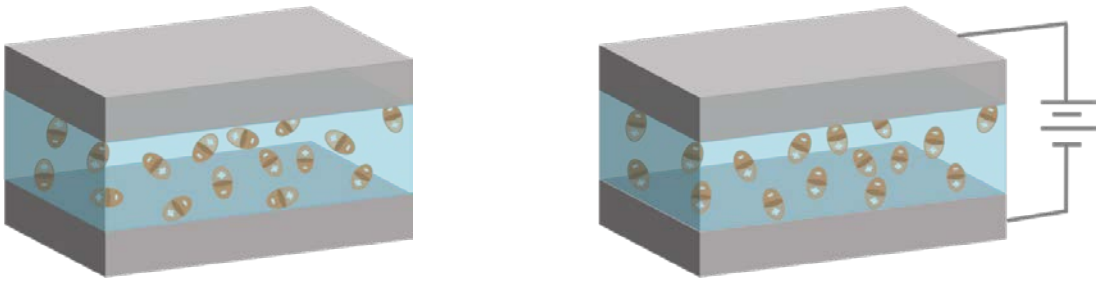

Figure 3. Schematic of rotation of dipole with the presence of electric field.

A parallel plate capacitor with an insulated material inserted between the plates is a direct example to illustrate the dielectric property. In the presence of electric field, the dipoles inside the materials are aligned as shown in Figure 3. The defining equation of dielectric constant is:

$$D_m = \varepsilon_{mn} E_n \tag{2-4}$$

$$E_n = \beta_{nm} D_m \tag{2-5}$$

where the subscripts m, n are the directions of that element, D_m (C/m^2) is the electric displacement, ε_{mn} (F/m) is the dielectric constant, and E_n (V/m) is the electric field. Another parameter that is more commonly used than the dielectric constant is permittivity, also known as relative dielectric constant ε_r. It is defined as below:

$$\varepsilon_r = \frac{\varepsilon}{\varepsilon_0} \tag{2-6}$$

where ε_0 is the dielectric constant in vacuum condition with the value of 8.85×10^{-12} (F/m). The larger the permittivity, the stronger the rotation response of the dipoles will occur.

2.2.3 Piezoelectric coefficient

Piezoelectric coefficients are used for representing the ability of a piezoelectric to produce charge when applying force, or measuring the deformation in the presence of electric field. Piezoelectric coefficients can thus be described in terms of electric displacement *D*, electric field *E*, strain *S* and stress *T* (Moulson & Herbert 1990)

$$D_m = d_{mij} T_{ij} \tag{2-7}$$

$$D_m = e_{mij} S_{ij} \tag{2-8}$$

$$E_{ij} = -g_{ijm} T_m \tag{2-9}$$

$$E_{ij} = -h_{ijm} S_m \tag{2-10}$$

where *d (C/N)*, *e* (C/m^2), *g* (m^2/C), *h (N/C)* are 4 kinds of piezoelectric coefficients. The subscripts of the coefficients represent both electric field direction and mechanical field direction. For instance, d_{mij} indicates that the piezoelectric with electric polarization in *m* direction, is loaded with a stress in *ij* direction. The equations above describe the direct piezoelectric effect. For the indirect piezoelectric effect, the mechanical variables (*T, S*) are described in terms of electrically-independent variables (*D, E):*

$$S_{ij} = d_{ijm} E_m \tag{2-11}$$

$$T_{ij} = -e_{ijm} E_m \tag{2-12}$$

$$S_{ij} = g_{ijm} D_m \tag{2-13}$$

$$T_{ij} = -h_{ijm} D_m \tag{2-14}$$

These 4 types of piezoelectric coefficients are obtained from different boundary conditions, and are used depending on the specific circumstances. The most commonly used parameters are d_{33} or d_{31}. The d_{33} constant describes the electric polarization generated in the 3 direction as the stress is applied in the 3 direction, which is also known as the longitudinal coefficient. In some other applications, where the electric polarization of the piezoelectric material is perpendicular to the direction of applied force, the coefficient d_{31} is used, which is called the transverse coefficient. By measuring current as a function of stress, d_{33} and d_{31} are more accessible to researchers. In particular, they are used to compare the piezoelectric responses of different materials in terms of unit stress applied. For example, the d_{33} of soft $PbZrTiO_3$ is about 417 (pC/N), while for a lead-free material $Na_{0.5}Bi_{4.5}Ti_4O_{15}$, the value is only 18 (pC/N) (Turner et al. 1994). For the application of energy harvesting, higher piezoelectric coefficients are desired.

The piezoelectric voltage coefficient g is used in generator or sensing applications. Ryu et al. (2001) focus on the g_{31} of PZT as a strain source or electrical signal source in the application of a magnetoelectric composite, where the output voltage of piezoelectric element is concerned.

2.2.4 Electromechanical coupling factor

As the piezoelectric materials transfer mechanical energy to electric work, or produce mechanical work with the input of electricity, the parameters used to describe the efficiency of this process is the electromechanical coupling factors. These are defined as “non-dimensional

coefficients which characterize the efficiency of transforming the stored energy into mechanical or electric work of a particular piezoelectric material under a specific stress and electric field configuration" by IEEE Standard 176-1987 (Rosen et al. 1992). These coefficients are also known as quasi-static material coupling factors, which can be expressed as

$$k_{ij}^2 = \frac{W_c}{W_t} \tag{2-15}$$

where W_c is the converted work, and W_t is the total work the piezoelectric produce; i represents the direction of the applied electrodes and j is the direction of the applied or developed mechanical energy. Note that k_{ij} exclusively depends on the piezoelectric material properties. In order to compare different interfaces that are used to store energy generated by any piezoelectric material, the effective coupling factor can be used:

$$k_{eff}^2 = \frac{\omega_{oc}^2 - \omega_{sc}^2}{\omega_{oc}^2} \tag{2-16}$$

where ω_{oc} is the angular resonance frequency of the open-circuit structure, and ω_{oc} is the angular resonance frequency of the short-circuit structure. Based on previous reports (Renaud et al. 2007; Guyomar et al. 2005), k_{eff}^2 is in range 0.01 to 0.1 for real interfaces coupling with a piezoelectric material.

2.2.5 Mechanical quality factor

For most of the applications of piezoelectric harvesters or sensors, the working frequency is not exactly the same as the resonance frequency, where the optimal performance of the harvester may occur. Mechanical quality factor is a parameter to show how underdamped the harvester is when it is vibrating, within the frequency bandwidth relative to its resonant

frequency. Mechanical quality factor represents the ratio of the relationship between stored energy and dissipated energy of the vibration system in every cycle, and it can be expressed as below:

$$Q = 2\pi \frac{E_{stored}}{E_{lost\ per\ cycle}} \tag{2-17}$$

Mechanical quality factor can be measured through response spectrum of the resonant circuit. A typical impedance spectrum of a piezoelectric energy harvester is shown here as an example (Figure 4) (Sherrit & Mukherjee 2007). The Q factor of the energy harvester can then be calculated as the ratio of the resonant frequency and the bandwidth of -3dB frequencies. It could be expressed as

$$Q_b = \frac{f_b}{f_{b2} - f_{b1}} \tag{2-18}$$

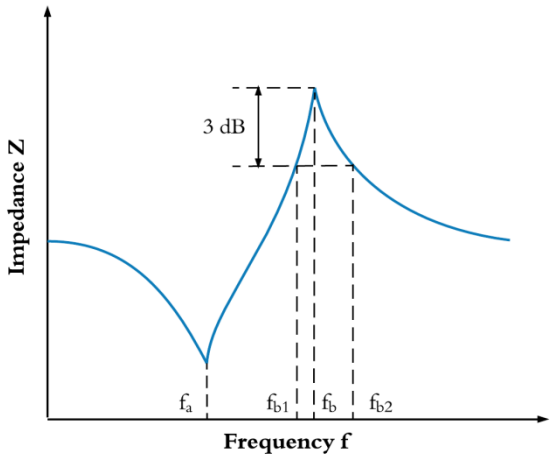

Figure 4. Diagram of impedance spectrum of typical piezoelectric energy harvester

2.2.6 Complex coefficients

Complex material coefficients have been found to model the piezoelectric systems more accurately for the consideration of phase shift in the AC response of piezoelectric materials (Alemany et al. 1994; Berlincourt et al. 1964). For a general linear system subjected to an AC input $x = Xe^{i\omega t}$, the response y can be expressed in terms of the input:

$$y = tXe^{i\omega t} \tag{2-19}$$

where the *t* is the term relating the input and the output. When *t* is real, then *y* and *x* are said to be in phase. On the other hand, when *t* is complex and $\boldsymbol{t} = t_r + it_i$, then *y* and *x* are out of phase by a phase angle φ, which can be expressed as:

$$y = |t|Xe^{i\omega t+\varphi} \tag{2-20}$$

where $|t| = \sqrt{({t_r}^2 + {t_i}^2)}$, the phase $\varphi = arctan(t_i/t_r)$.

Similarly, in the stress-strain relationship, to describe the propagation and dissipation of acoustic waves in a material, the complex elastic stiffness is used (McSkimin & Andreatch Jr 1967):

$$c = c_r + ic_i \tag{2-21}$$

Consequently, the mechanical quality factor Q can be derived in terms of the complex stiffness as below:

$$Q = \frac{c_i}{c_r} \tag{2-22}$$

In the dielectric community, it is common to use complex permittivity to model the material, so that the data reported addresses both dielectric constant and dielectric dissipation. The complex permittivity is written as:

$$\kappa = \frac{\varepsilon_r}{\varepsilon_0}\left(1 + i\frac{\varepsilon_i}{\varepsilon_r}\right) = \frac{\varepsilon_r}{\varepsilon_0}(1 + i\ tan\delta) = \kappa_r + i\kappa_r \tag{2-23}$$

where $tan\delta$ is the dissipation. It can also be translated as the ratio of leakage current to the charging current, in terms of conductivity ϑ and complex permittivity for a linear dielectric, under an electric field $\boldsymbol{E} = Ee^{i\omega t}$:

$$tan\delta = \frac{\varepsilon_i + \vartheta/\omega}{\varepsilon_r} \tag{2-24}$$

Considering the loss component of the piezoelectric coefficient for various materials, the electric displacement as a function of AC stress could be described by (Wang et al. 1993):

$$D_m = \left(d_{mpq,r} + id_{mpq,i}\right)T_{pq}e^{i\omega t} = \left|d_{mpq}\right|T_{pq}e^{i(\omega t+\theta_d)} \tag{2-25}$$

And for the indirect effect, the strain behaves as:

$$S_{pq} = \left(d_{mpq,r} + id_{mpq,i}\right)E_m e^{i\omega t} = \left|d_{mpq}\right|E_m e^{i(\omega t+\theta_d)} \tag{2-26}$$

Thus, the electromechanical coupling factor k_{ij}^2 in terms of electric, elastic and piezoelectric coefficient could be rewritten in complex form, which indicates that there is a phase difference between total input energy and the converted energy of the piezoelectric system. The total phase angle is derived as:

$$\theta_k = 2\theta_e - \theta_{c^D} - \theta_{\varepsilon^S} \tag{2-27}$$

where the subscripts e, c^D, ε^S are piezoelectric coefficient, elastic compliance measured under constant electric displacement D and permittivity under constant strain S, respectively.

2.3 CONSTITUTIVE EQUATIONS

Knowing the various coefficients of piezoelectric material, a thermodynamic potentials model is used to derive the governing equation of piezoelectric effect. The diversity of derivation is due to different choices of potentials and independent variables. Giving one of them as an example, the elastic Gibbs function under the isothermal and adiabatic condition can be given as

$$G_1 = \frac{1}{2}\left(\beta_{mn}^{T} D_m D_n\right) - \frac{1}{2}\left(s_{ijkl}^{D} T_{ij} T_{kl} + 2 g_{nij} D_n T_{ij}\right) \tag{2-28}$$

where β is inverse permittivity, s is elastic compliance, g is piezoelectric voltage coefficient; stress T and electric displacement D are two independent variables in this equation; the independent variables situated at the superscripts mean that they are held constant when defining the coefficient.

The elastic Gibbs potential, based on the above equation, is equal to the difference between internal electric potential and external electric potential due to the piezoelectric effect as well as mechanical energy due to the inverse piezoelectric effect. The constitutive equations of piezoelectricity for this potential can be derived from the derivative of the elastic Gibbs function:

$$S_{ij} = -\frac{\partial G_1}{\partial T_{ij}} = s_{ijkl}^{D} T_{kl} + g_{nij} D_n \tag{2-29}$$

$$E_m = -\frac{\partial G_1}{\partial D_m} = \beta_{mn}^{T} D_n - g_{nij} T_{ij}, \tag{2-30}$$

where S is the strain of the material, and E is the electric field. Based on Eq. (2-29), (2-2) and (2-13), the total strain of the piezoelectric material results from both applied stress and electric field. Via other thermodynamic potentials, the constitutive equations of piezoelectricity can be derived with varying independent variables and are

$$S_{ij} = s^E_{ijkl} T_{kl} + d_{ijm} E_m \tag{2-31}$$

$$D_m = \varepsilon^T_{mn} E_n + d_{ijm} T_{ij} \tag{2-32}$$

and

$$T_{ij} = c^E_{ijkl} S_{kl} - e_{ijm} E_m \tag{2-33}$$

$$D_m = \varepsilon^S_{mn} E_n + e_{ijm} S_{ij} \tag{2-34}$$

and

$$T_{kl} = c^D_{ijkl} S_{kl} - h_{klm} D_m \tag{2-35}$$

$$E_m = \beta^S_{mn} D_n - h_{ijm} S_{ij}\,, \tag{2-36}$$

where *d, e, h* are piezoelectric coefficients, *c* is the elastic stiffness, *ε* is the permittivity of the material. These relationships can be represented using matrix form to include all the constants and variables in all directions. For instance, the Eq.(2-31) and (2-32) are also known as

$$\begin{bmatrix} S_1 \\ S_2 \\ S_3 \\ S_4 \\ S_5 \\ S_6 \\ D_1 \\ D_2 \\ D_3 \end{bmatrix} = \begin{bmatrix} s^E_{11} & s^E_{12} & s^E_{13} & s^E_{14} & s^E_{15} & s^E_{16} & d_{11} & d_{12} & d_{13} \\ s^E_{21} & s^E_{22} & s^E_{23} & s^E_{24} & s^E_{25} & s^E_{26} & d_{21} & d_{22} & d_{23} \\ s^E_{31} & s^E_{32} & s^E_{33} & s^E_{34} & s^E_{35} & s^E_{36} & d_{31} & d_{32} & d_{33} \\ s^E_{41} & s^E_{42} & s^E_{43} & s^E_{44} & s^E_{45} & s^E_{46} & d_{41} & d_{42} & d_{43} \\ s^E_{51} & s^E_{52} & s^E_{53} & s^E_{54} & s^E_{55} & s^E_{56} & d_{51} & d_{52} & d_{53} \\ s^E_{61} & s^E_{62} & s^E_{63} & s^E_{64} & s^E_{65} & s^E_{66} & d_{61} & d_{62} & d_{63} \\ d_{11} & d_{12} & d_{13} & d_{14} & d_{15} & d_{16} & \varepsilon^T_{11} & \varepsilon^T_{12} & \varepsilon^T_{13} \\ d_{21} & d_{22} & d_{23} & d_{24} & d_{25} & d_{26} & \varepsilon^T_{21} & \varepsilon^T_{22} & \varepsilon^T_{23} \\ d_{31} & d_{32} & d_{33} & d_{34} & d_{35} & d_{36} & \varepsilon^T_{31} & \varepsilon^T_{32} & \varepsilon^T_{33} \end{bmatrix} \begin{bmatrix} T_1 \\ T_2 \\ T_3 \\ T_4 \\ T_5 \\ T_6 \\ E_1 \\ E_2 \\ E_3 \end{bmatrix} \tag{2-37}$$

This matrix is the general form of the constitutive equation of the direct and indirect piezoelectric effects.

For some piezoelectric materials, many elements of the matrix in Eq. (2-37) are zero because of the symmetry of the crystal structure. Based on experiment results, for PZT with

direction 3 (thickness direction) of polarization, T_1, T_2, and T_3 can produce electric displacement in only direction 3; And T_5 (or T_4) generates piezoelectric effect in only direction 1 (or 2); T_6 has no piezoelectric effect. Only two independent free (constant stress) permittivity ($\varepsilon_{11}^T = \varepsilon_{22}^T$, ε_{33}^T) are enough for the dielectric property of the material, and only five independent short-circuit ($E = 0$) elastic compliance coefficients ($s_{11}^E = s_{22}^E$, s_{33}^E, $s_{44}^E = s_{55}^E$, $s_{66}^E = 2(s_{11}^E - s_{12}^E)$, $s_{12}^E = s_{21}^E$, $s_{13}^E = s_{23}^E$) are used. Therefore, the reduced form of Eq. (2-37) of PZT can be finally expressed as:

$$\begin{bmatrix} S_1 \\ S_2 \\ S_3 \\ S_4 \\ S_5 \\ S_6 \\ D_1 \\ D_2 \\ D_3 \end{bmatrix} = \begin{bmatrix} s_{11}^E & s_{12}^E & s_{13}^E & 0 & 0 & 0 & 0 & 0 & d_{31} \\ s_{12}^E & s_{11}^E & s_{13}^E & 0 & 0 & 0 & 0 & 0 & d_{31} \\ s_{13}^E & s_{13}^E & s_{33}^E & 0 & 0 & 0 & 0 & 0 & d_{33} \\ 0 & 0 & 0 & s_{44}^E & 0 & 0 & 0 & d_{15} & 0 \\ 0 & 0 & 0 & 0 & s_{44}^E & 0 & d_{15} & 0 & 0 \\ 0 & 0 & 0 & 0 & 0 & 2(s_{11}^E - s_{12}^E) & 0 & 0 & 0 \\ 0 & 0 & 0 & 0 & d_{15} & 0 & \varepsilon_{11}^T & 0 & 0 \\ 0 & 0 & 0 & d_{15} & 0 & 0 & 0 & \varepsilon_{11}^T & 0 \\ d_{31} & d_{31} & d_{33} & 0 & 0 & 0 & 0 & 0 & \varepsilon_{33}^T \end{bmatrix} \begin{bmatrix} T_1 \\ T_2 \\ T_3 \\ T_4 \\ T_5 \\ T_6 \\ E_1 \\ E_2 \\ E_3 \end{bmatrix} \quad (2\text{-}38)$$

Ideally, with the constants in the equation above, the piezoelectric behavior under the application of electric field, current, stress, and strain can be predicted. While in practice, most piezoelectric materials have non-linearity, dispersion, and energy losses. For more accurate characterization, the coefficients should be expressed as a function of frequency ω, electric field E_i, stress T_{ij}, temperature T, and time t:

$$s_{kl}^E = s_{kl,r}^E(\omega, E_i, T_{ij}, T, t) + i s_{kl,i}^E(\omega, E_i, T_{ij}, T, t) \quad (2\text{-}39)$$

$$d_{ij} = d_{ij,r}(\omega, E_i, T_{ij}, T, t) + i d_{ij,i}(\omega, E_i, T_{ij}, T, t) \quad (2\text{-}40)$$

$$\varepsilon_{ij}^T = \varepsilon_{ij,r}^T(\omega, E_i, T_{ij}, T, t) + i \varepsilon_{ij,i}^T(\omega, E_i, T_{ij}, T, t) \quad (2\text{-}41)$$

This generalized representation takes account of these five factors, which are of importance in some cases: (1) The dielectric and piezoelectric coefficients are frequency dependent due to different polarization mechanisms in different frequency zones. (2) Most of the practical materials used for transducer are temperature dependent, especially ferroelectric, which has a curie point for temperature, where the piezoelectric and dielectric constants change dramatically. Chapter 5 will have a detailed discussion on ferroelectric and Curie point. (3) The application of electric field on the piezoelectric sample is a common treatment called poling. With different poling conditions, the piezoelectric coefficients vary a lot. (4) Operation of the sample at high stress and high electric field may result in partial depolarization of the sample, which will affect the piezoelectric coefficients substantially. (5) The piezoelectric property of the material decays with time exponentially after the poling process, which is described by an aging curve. Therefore, care should be taken when assuming the piezoelectric materials studied are lossless, linear and frequency independent.

3.0 PIEZOELECTRIC ENERGY HARVESTER AND INTERFACE CIRCUITS

In this chapter, we review how the piezoelectric property of materials is utilized to harvest kinetic energy from the ambient environment.

Notably, the harvested power as well as the efficiency are strongly dependent on excitation frequency due to the piezoelectric element outputting the maximum power at its resonance frequency. Generally, the frequency range of typical environmental sources is less than 200Hz: the vibration source of machinery is often within the range of 100 ~ 200Hz, and the frequency range of human or animal motion is much lower (1~30Hz) (Roundy et al. 2003).

On the other hand, the commonly used piezoelectric ceramic devices have much higher fundamental frequencies that lie in the kilo-Hertz range. Therefore, other than choosing materials that have lower resonant frequency, a variety of designs of harvesters configurations and circuitry have been employed to lower the system resonant frequency.

Here, three common configurations of the piezo-element parts for low-frequency application are introduced, and the basic theory of interface circuits is discussed.

3.1 DIFFERENT CONFIGURATIONS OF ENERGY HARVESTER

3.1.1 Unimorph and bimorph cantilever configuration

The cantilever structure is the simplest in piezoelectric harvesters. Two layers of metal electrodes are deposited on the two surfaces of a thin piezo-element. As shown in Figure 5(a), one end of the cantilever stack is fixed by mounting on the excitation source and the other end is free (Khan & Ahmad 2016). This flexible vibration mode has much lower resonance frequency than other modes of the piezoelectric element. Additionally, to achieve higher power output, two layers of piezoelectric element are attached to each other and assembled into the stack to form a bimorph cantilever.

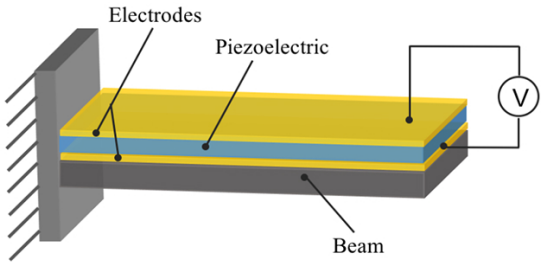

Figure 5. (a) Unimorph structure of cantilever configuration (Khan & Ahmad 2016).

Figure 6 show two connection types of the bimorph structure. The small arrows show the polling direction of the piezoelectric element. Two piezo-layers with opposite polarization in (a) are connected in series, which produces twice the output voltage and equal current as the case of

a unimorph cantilever, whereas the capacitance is divided in half. Another type is parallel connection of the two piezo-layers with the parallel polling direction (Shown in Figure 6(b)). Under this connection, the output voltage of the cantilever stays the same as in a unimorph structure, but the current and the capacitance are doubled. It should be mentioned that the converted output power is not affected by the layer connection type, which only makes a difference to the ratio of voltage to current.

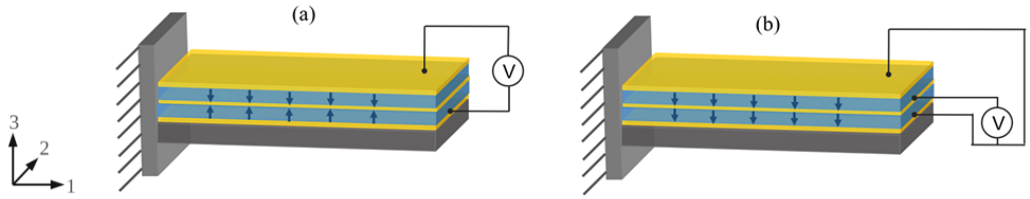

Figure 6. (a) Bimorph structure in series of cantilever configuration; (b) Bimorph structure in parallel of cantilever configuration (Hehn & Manoli 2015).

The piezoelectric mode of unimorph and bimorph cantilevers is '31' mode since the strain excited is in the '1' direction and the output voltage is in the '3' direction, thus a d_{31} constant is used to characterize the harvester. However, for most piezoelectric materials, the value of d_{31} is twice smaller than d_{33} considering the fact that the poling axis is in the 3 direction (Rosen et al. 1992). To employ the 33 mode in a cantilever structure, interdigitated electrodes are designed (Show in Figure 7(a) (Li et al. 2014)). An array of alternating negative and positive electrodes is deposited on the surface for polling and harvesting, so that the polarization direction is lateral, which is parallel to the strain direction.

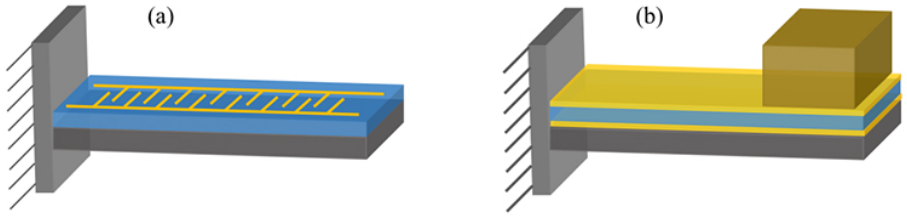

Figure 7. Unimorph piezoelectric cantilever with (a) interdigitated electrodes; (b) proof mass on the tip. (Li et al. 2014)

Often, to further lower the fundamental frequency of the cantilever, a proof mass is added to the end of the beam to increase the strain as shown in Figure 7(b) (Li et al. 2014). With the participation of a tip mass, the output power is enlarged and the resonance frequency is adjustable by controlling the value of the mass.

3.1.2 Cymbals (Discs, Diaphragms)

Cymbal structure consists of one piezoelectric disc and two metal end-caps attached to the disc on either side. Due to the dome-shape structure of the metal shown in Figure 8 (Hongduo et al. 2010), the piezoelectric disc is compressed as well as stretched by the dome when an axial force is applied. Thus, both 33 and 31 vibration modes of the disc are involved in the charge generation. The effective piezocoefficient of the cymbal harvester can be expressed as (Kim et al. 2005):

$$d_{eff} = d_{33} + A|d_{31}| \tag{3-1}$$

where A is the amplification factor between the input axial force on the end-caps and the converted radial force applied on the piezo-disc.

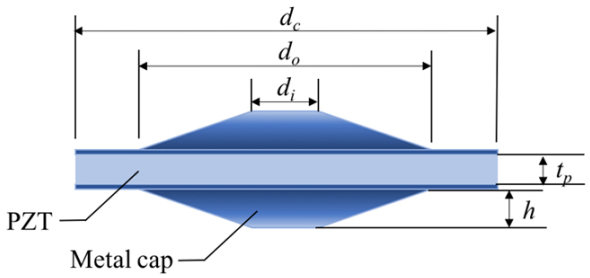

Figure 8. Structure of cymbal harvester with annotation of key parameters. (Hongduo et al. 2010)

The end-caps of the cymbal harvester are usually made of steel with high yield strength, and therefore this harvester can withstand high impulse forces. Additionally, owing to the circular dome shape of the end-caps, stress distributes on the disc more uniformly than on a cantilever. Both facts result in higher power output from the cymbal harvester than from a cantilever energy scavenger. A further increase of the output power can be obtained by optimizing the geometry parameters (i.e. t_p, d_c, d_o, d_i in the Figure 8) of the cymbal and the end-caps. For instance, a cymbal with d_c = 29mm and t_p = 1, a 39mW output power can be obtained as it is subjected to a 7.8N AC force in 100Hz (Kim et al. 2005).

It should be noted that, however, the robust nature of the metal end-caps results in less efficiency in harvesting low-level excitation forces, and the optimal frequency is still beyond the range of human motion.

3.1.3 THUNDER-type arch configuration

THUNDER® (thin-layer composite unimorph ferroelectric driver and sensor) refers to a type of curved high-performance piezoelectric actuator originally developed by NASA. There are 5 layers in the THUNDER structure that are shown in Figure 9 (Aimmanee & Hyer 2004).

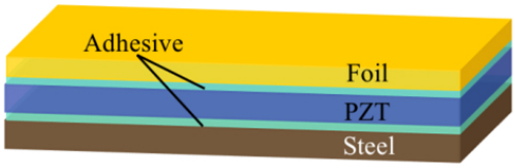

Figure 9. Schematic of the cross-section of a THUNDER (Aimmanee & Hyer 2004).

The middle layer is piezo-ceramic PZT layer and is attached to two metallic alloy electrodes on each side by using two adhesive layers. The substrate electrode layer is made of steel, and an aluminum alloy is usually employed to build the superstrate electrode layer. The five constituent layers are heated to 204 ℃ and then pressurized by 241.3kPa N_2 gas with a further elevation of temperature. After heating, the stack is cooled to room temperature, during which the internal stress between ceramic and two metallic layers is produced due to the inter-layer mismatch in the coefficient of thermal expansion (CTE) (Kim et al. 2009). These residual stresses cause a curve configuration as shown in Figure 10.

Similar to the cymbal harvester, the vibration mode of the piezoelectric layer in the THUNDER is both 31 (as majority) and 33 mode. Comparing to cantilever structure, the yield strength of the THUNDER is considerably higher and it can spring back to the curved shape after

each deformation. The metallic layers of THUNDER are much more flexible than the ones of cymbal. Therefore, a much lower force applied is needed to deform the THUNDER than the cymbal.

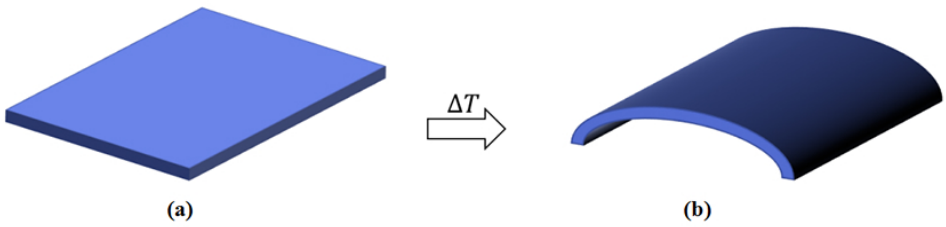

Figure 10. Structure of THUNDER (a) in initial condition and (b) after cooling. (Aimmanee & Hyer 2004)

Featured by large deformation and high yield strength, THUNDER has extraordinary strength in harvesting human motion of which the frequency and magnitude of force is low, while the displacement range is large. Shenck and Paradiso (Shenck & Paradiso 2001) developed a bimorph THUNDER with size of 5cm × 5cm × 15μm and installed it in a shoe insole to harvester the energy from human walking. A maximum output power of 8.4mW was obtained with 500 kΩ resistor load.

3.2 ANALYSIS OF INTERFACE CIRCUITS

3.2.1 Electromechanical modeling of harvesters

To study the coupling between the aforementioned piezoelectric element and the interface circuit, the equivalent circuit of the former part has to be built. Normally, a kinetic energy harvester is modeled as a second-order spring-mass-damper system. Using lumped elements of stiffness k_s of the spring, damping coefficient d of the damper and a seismic mass m as well as the transducer connected to the interface circuit, the model of the energy harvester system is found to characterize the physical behavior of the system and is shown in Figure 11 (Mitcheson et al. 2004; Shu & Lien 2006; Williams & Yates 1996).

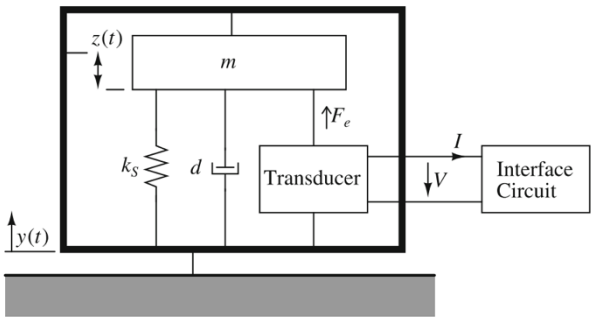

Figure 11. Mechanical modeling of the piezoelectric energy harvester (Mitcheson et al. 2004; Shu & Lien 2006; Williams & Yates 1996).

The electrical output can be derived from the constitutive equations of piezoelectricity, when considering the variables of the macroscopic geometric and electric parameters of the harvester lead to the governing equation which are (Hehn & Manoli 2015):

$$\begin{cases} ma = m\ddot{z} + d\dot{z} + kz + \Gamma V_P \\ I = \Gamma\dot{z} - C_P\dot{V}_P \end{cases} \tag{3-2}$$

where Γ is the generalized electromechanical coupling factor; C_P is the capacitance of the piezoelectric material; V_P is the open-circuit voltage from the material. Alternatively, the equivalent circuit of the piezoelectric element revealing the electro-mechanical coupling can be found by using the analogy rule between mechanical and electrical components (See upper left equations Figure 12) (Renaud et al. 2008; Kong et al. 2010).

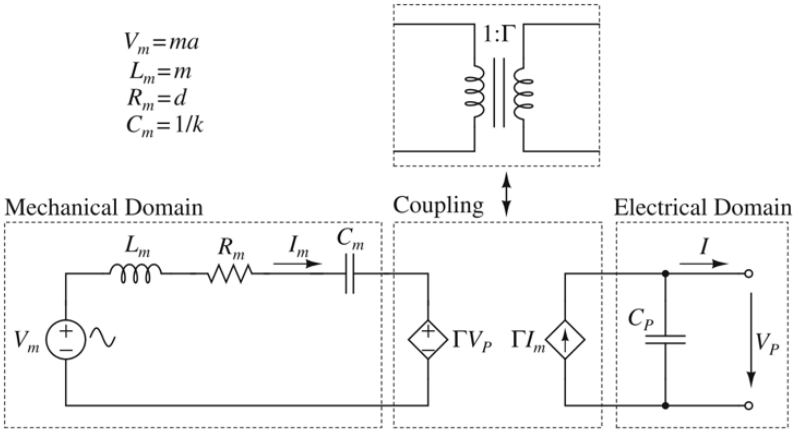

Figure 12. Equivalent circuit of the piezoelectric element. (Renaud et al. 2008; Kong et al. 2010)

For circuitry study, only the electric domain part of the equivalent circuit is used to evaluate the performance of the interface circuit, which is shown in Figure 13 (Hehn & Manoli 2015). A sinusoidal current source is used to model the harvester under vibration. Note that the parallel resistor is the resistance of the material representing the dielectric loss, which is often omitted (see Figure 13 (a)) due to the extremely high value resistance (larger than 10MOhm).

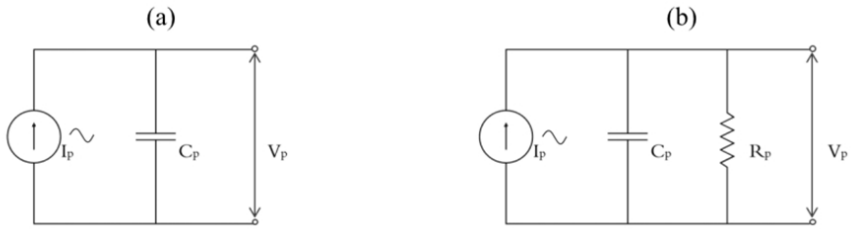

Figure 13. Simplified equivalent circuit of the piezoelectric element for circuitry study (a) omitting leaking loss of piezoelectric element; (b) with consideration of resistance of the piezoelectric element. (Hehn & Manoli 2015)

3.2.2 Analysis of common interface circuits

i. Resistor load

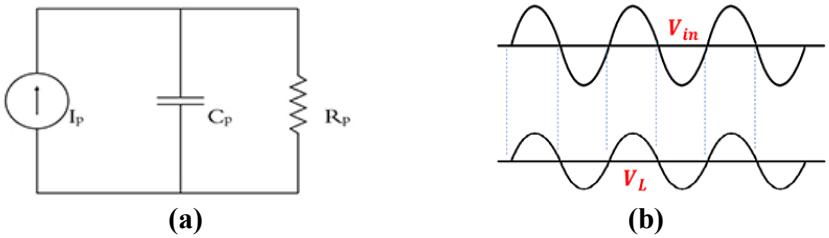

Figure 14. (a) The diagram of resistor load connecting with piezoelectric element; (b) The waveform of output power as well as the displacement of the piezoelectric element (Guyomar et al. 2007).

The resistor load can be considered as the simplest "interface circuit" by directly adding a load component to the output of the piezoelectric element. The diagram and a typical waveform of load voltage is shown in Figure 14. There is no phase shift between the vibration displacement *u* and the output voltage *V* in this example. The voltage on the load resistor stays sinusoidal with change in magnitude of peak value when the resistance of load varies, and thereby the output

power is not constant for different resistor load. Therefore, the resistor load circuit is usually used to characterize the piezoelectric element in terms of the output power as well as the frequency response, even though the resistor load is not practical for the application of real energy harvesters with the absence of a storage element.

ii. Full-wave rectifier

The diagram of a piezo-element connected to the full-wave rectifier circuit is shown in Figure 15. It is a simple method to convert AC power source to DC type through a bridge configuration of 4 diodes. For positive cycle, D1 and D4 are forward-biased and current flows from point *a* to *b*; for negative cycle, D3 and D2 are connected, the current still flows from point *a* to *b,* so there is only one direction of current flow into the load component. Since the diodes are passive electrical components, there is no need for external power to operate the rectifier. Hence this circuit is common in the real energy harvester applications.

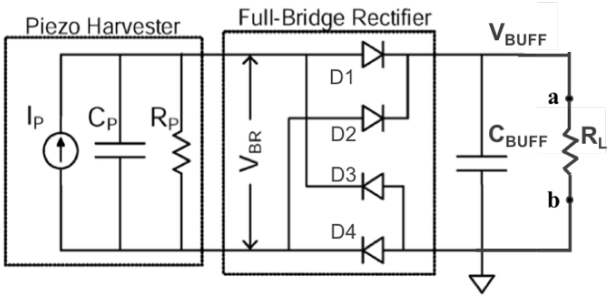

Figure 15. The diagram of full-wave rectifier load connecting with piezoelectric element (Hehn & Manoli 2015).

If the load part of the full-wave rectifier is only resistive, the waveform of the voltage at the load flips the negative cycle of the AC source to the positive cycle. But a buffer capacitor is

often added in parallel to the load resistor to regulate the load voltage to be a constant value as shown in Figure 15. The buffered load voltage is labeled as V_{BUFF}.

With the presence of the buffer capacitor, the output voltage of the harvester V_{BR} is shown in Figure 16 ((Ramadass 2009). The diodes are reverse-biased until the output voltage V_{BR} reaches the V_{BUFF}, and thus the waveform of output voltage is clipped at the value of V_{BUFF}. This means, however, that the rectifier blocks the output power from the piezoelectric when the corresponding V_{BR} is less than V_{BUFF}. The waveform of input current source i_P is also provided in Figure 16, where the shaded area represents the charge that is not delivered to the load every half-cycle.

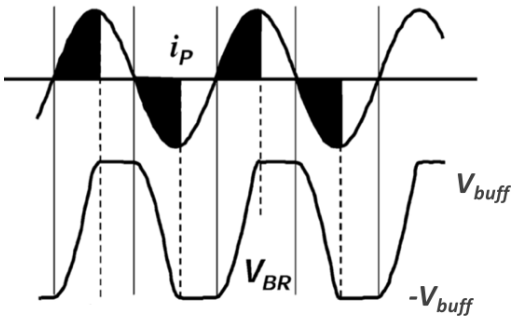

Figure 16. The waveform of input current on the top; and output voltage of the piezoelectric element on the bottom under full-wave rectifier.(Ramadass 2009)

iii. Voltage doubler

Similar to the full-wave rectifier, voltage doubler circuit, which is shown in Figure 17, converts AC type of power source to DC type by using two diodes either in series or in parallel

to the load. Also, when a buffer capacitor is parallel to the resistive load, some portion of the output power from the piezoelectric element is blocked by the rectifier.

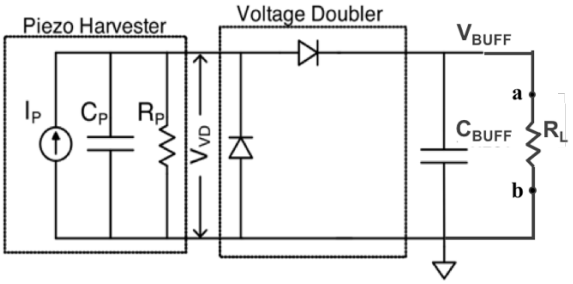

Figure 17. The diagram of voltage doubler connecting with piezoelectric element (Ramadass 2009)

The waveform of the input current i_P and the output voltage V_{VD} is presented in Figure 18. In the positive cycle of the input current, the V_{VD} is firstly increase and then levels out at V_{BUFF}. In the negative cycle, no current flows to charge the capacitor even though the diode is on the forward-biased state. Thus, the V_{VD} is maintained at a level close to 0 (the generated charge is grounded). This half-cycle grounded design is the reason why there is less work needed to fully charge the capacitor from 0 to V_{BUFF} in the positive cycle, instead of from $-V_{BUFF}$ to V_{BUFF}.

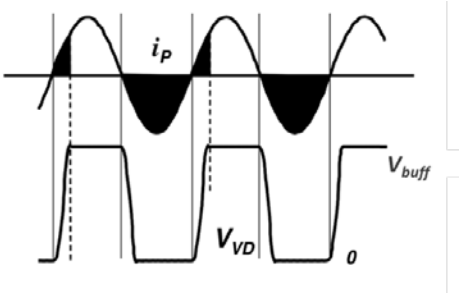

Figure 18. The waveform of input current on the top; and output voltage of the piezoelectric element on the bottom under voltage doubler. (Ramadass 2009)

iv. Synchronized-Switch Harvester (SSH) Resistance load

Due to the large power loss in both full-wave and voltage-doubler rectifier circuits, another interface circuit called Synchronized-Switch Harvester (SSH) is designed to improve the portion of transferred power. Inspired by the grounded design of voltage-doubler, this configuration makes use of a switch between the piezoelectric element and the full-wave rectifier as shown in Figure 19. As the switch is closed for a brief time, the piezoelectric element is shorted and the charge generated is grounded immediately.

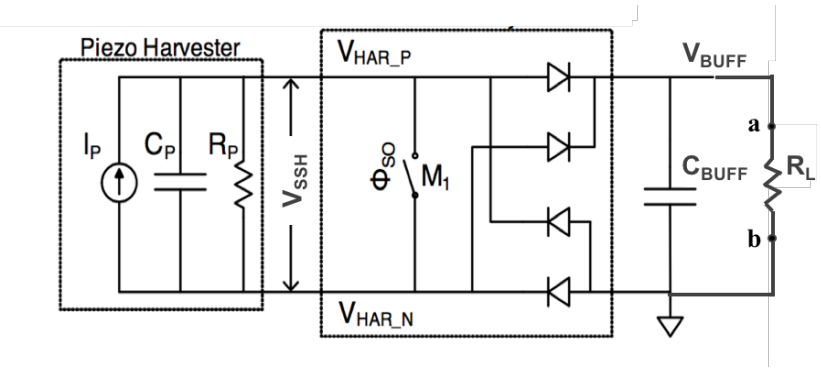

Figure 19. The diagram of SSH connecting with piezoelectric element (Ramadass 2009)

The waveform of input current i_P, output voltage V_{SSH} and the switch control signals that are involved with SSH circuit are shown in Figure 20. If the switch is controlled to close for a brief time at the moment when input current changes its polarity (crosses zero), it can be observed that there is an acceleration in the process by which V_{SSH} increases to V_{BUFF} by charging C_P from 0 instead of the maxima of negative i_P, and thereby a reduction in the shaded

area marked in the input current waveform comparing to the last two configurations. Therefore, a higher power collected by the circuit is expected.

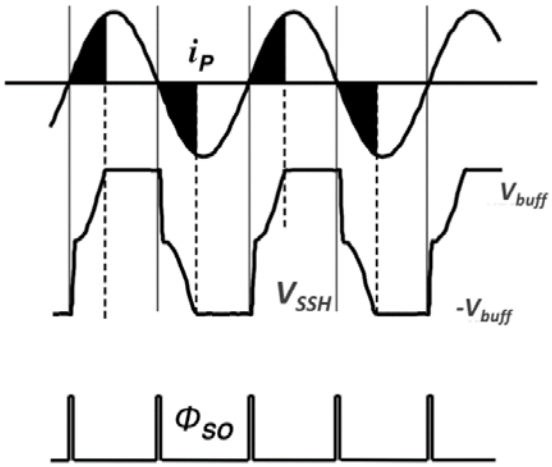

Figure 20. The waveform of input current on the top and output voltage of the piezoelectric element on the bottom under SSH circuit (Ramadass 2009).

A final iteration on the line of circuits described herein is the development of synchronized-switch-harvester-with-inductor (SSHI) circuit (Badel 2006). This circuit will not be covered in this thesis because the application of SSHI lies in a high frequency range.

4.0 SYNCHRONIZED-MECHANICAL-SWITCH HARVESTER (SMSH)

4.1 MOTIVATION

After analyzing the strength of Synchronized-Switch Harvester (SSH) and the improvement of output power that it can realize, an experimental setup was built and studied for SSH. The first challenge is that the implementation of the electronic switch requires a gate-driven circuitry and an externally powered microcontroller is needed for the switch-control circuit(Shen et al. 2011).

Secondly, the closing of the switch is synchronized with the polarity change of the input current, i.e. the instant when the output open-circuit voltage V_{OC} achieves maxima due to the capacitive nature of the piezoelectric element. However, the detection of maxima of V_{OC} is impractical because an energy storage component and electronic load are connected to the piezoelectric element in real applications. Thus, with the assumption that the mechanical displacement and the output voltage are in-phase around the resonant frequency (Flatau et al. 2004), it is the maxima of magnitude of displacement that is measured to correspond to the maximum of output voltage so the signal of maxima of displacement is used to trigger the switch. Therefore, the switch closes when the vibration displacement of the piezoelectric element achieves its maxima in both directions. Here, a displacement sensor is employed to determine the accurate time when the switch closes.

A typical experiment setup for SSH is shown in (Lefeuvre 2006). The PZT patches are attached to a steel beam to form the piezoelectric cantilever. The electromagnet in the setup driven by the function generator and amplifier provides continuous vibration excitation for the piezoelectric cantilever. A displacement detector is placed at the free end of the cantilever to monitor the vibration magnitude of the beam and is connected to the switch control circuit. The displacement detector sends a signal to trigger the switch closure as the beam achieves a maximum displacement in either direction.

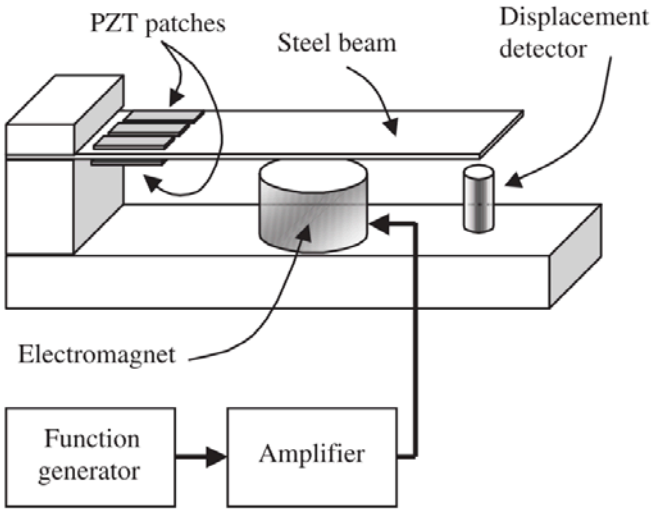

Figure 21. Sketch of the typical experiment setup for building SSH with displacement sensor (Lefeuvre 2006).

As an energy generator, a harvester system that needs a power source will weaken the efficiency of the transducer. On the other hand, the need of displacement sensor will not only increase the power consumption of the circuitry, but is also adverse to the trend of miniaturizing of the electronics. Therefore, achieving the synchronized-switch technique without an external power supply or a displacement sensor is one of the motivations of this thesis.

4.2 INTRODUCTION OF SYNCHRONIZED-MECHANICAL-SWITCH HARVESTING (SMSH)

Here we introduce a concept of using a mechanical switch to replace the electrical switch in SSH, and thereby overcoming the aforementioned issues that exist in the current SSH.

(a) **(b)**

Figure 22. Schematic of SMSH with vibrating piezoelectric element reach (a) minimum position; (b) maximum position.

Figure 22 is the schematic of the mechanical switch structure for a piezoelectric element that deforms in 33 mode. The mechanical switch consists of two upper metallic contacts that straddle the upper (superstrate) piezoelectric electric electrode, and are attached to the other (substrate) electrode of the piezoelectric material. The upper two metallic contacts are set at the approximately maximum and minimum vibration positions of the superstrate electrode, respectively, where the switch is supposed to close. When the superstrate electrode reaches the maximum displacement, the piezoelectric element is thus grounded by contacting the upper metallic plate, which has been connected to the substrate electrode through the bottom metallic

contact. Likewise, when the electrode reaches the minimum displacement, the piezoelectric element is grounded.

Using this mechanical switch is a simple way to get rid of the power source for the electrical switch as well as the displacement sensor. Notably, two requirements for SMSH application are: 1) the material should be able to be deformed largely to ensure the switch stays open in the middle of the two metal contacts; 2) to avoid undesirable connection with the metal contact, no wrinkling is allowed on the electrodes of the piezoelectric material. According to these requirements, we chose two piezo-elements for SMSH application, which will be introduced in the end of the Chapter 5.0 after reviewing the common classes of piezoelectric materials.

The feasibility of this concept and the needed components in the setup for building an SMSH harvester will be illustrated in Chapters 6.0 and 7.0 . Furthermore, the performance of output power of SMSH within the low frequency range is also discussed.

5.0 MECHANISM OF PIEZOELECTRICITY IN MATERIALS

5.1 PIEZOELECTRICITY AND FERROELECTRICITY IN CERAMICS

5.1.1 Generation of piezoelectricity in crystalline

Piezoelectric ceramics are referred to as crystalline. For the piezoelectric effect to occur, the presence of a non-centrosymmetrical crystallographic symmetry is necessary. In 32 crystalline classes, 21 of them lack of a center of symmetry, and 20 of them show piezoelectricity. The asymmetry of crystal structure results in a deviation of equivalent positive and negative charges. Deformation of material can cause the ionic displacement, which builds the polarity of the structure, and triggers surface charge to balance this change to thus produce current.

Barium titanate, a typical piezoelectric ceramic, produces piezoelectric bias through this mechanism. A unit cell of $BaTiO_3$ crystal is shown in Figure 23 (Popovici et al. 2011). Taking size of real atoms into account, the whole lattice is an asymmetric structure. Since the atoms at the lattice corner (Ba^{2+}) are considerably larger than the central atom (Ti^{4+}), off-centering of an undersized atom (Ti^{4+}) within the O^{2-} octahedral allows the lattice to attain a stable bonding pattern. This deviation can be strengthened with the presence of electric field. This ionic

displacement results in an electric dipole as an origin of piezoelectricity. The arrow represents the polarity direction.

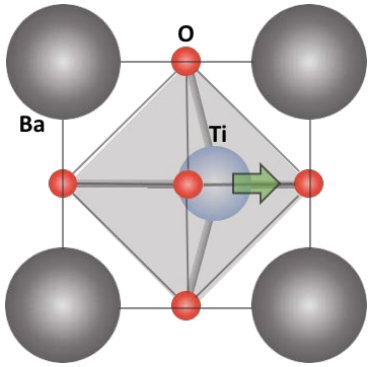

Figure 23. Representation of the ionic displacement in $BaTiO_3$ perovskite cell (Popovici et al. 2011)

The polarization in the crystal with application of stress under the assumption of linear condition, can be expressed as

$$P_i = d_{ijk}\sigma_{jk} \tag{5-1}$$

where d_{ijk} (C/N) is the piezoelectric coefficient. To fill in the subscripts with all 27 components, the explicit form of polarization in different directions is expressed as

$$P_1 = d_{111}\sigma_{11} + d_{112}\sigma_{12} + d_{113}\sigma_{13} + d_{122}\sigma_{22} + d_{123}\sigma_{23} + d_{133}\sigma_{33} \tag{5-2}$$

$$P_2 = d_{211}\sigma_{11} + d_{212}\sigma_{12} + d_{213}\sigma_{13} + d_{222}\sigma_{22} + d_{223}\sigma_{23} + d_{233}\sigma_{33} \tag{5-3}$$

$$P_3 = d_{311}\sigma_{11} + d_{312}\sigma_{12} + d_{313}\sigma_{13} + d_{322}\sigma_{22} + d_{323}\sigma_{23} + d_{333}\sigma_{33} \tag{5-4}$$

The piezoelectric material with off-centering structure before applying an electric field is known as **ferroelectrics**, in which the spontaneous dipole exists and can be reoriented. As a consequence of the presence of the spontaneous dipole, ferroelectric materials have permanent polarization which is compensated by free charge on the surface of the material. Ferroelectrics

have been a popular kind of piezoelectric materials to study in both academic and industrial fields.

5.1.2 Characterization of piezoelectric crystal material

5.1.2.1 Domain structure of ferroelectrics

Reorientation of spontaneous dipoles is related to the presence of domain structure. The space region where dipoles are aligned in one certain direction is called a domain (shown in Figure 24 (Fang et al. 2013)). Different domains pointing several directions can exist in one grain with the presence of domain walls, which are not the same as the grain boundaries.

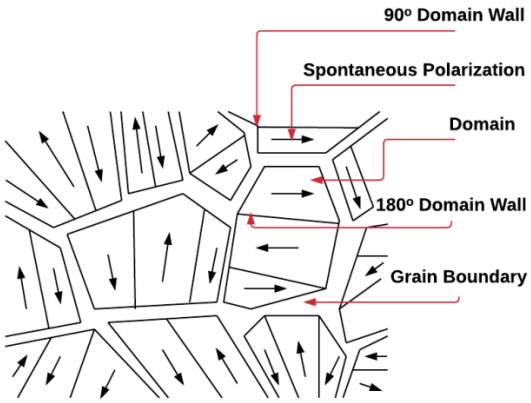

Figure 24. Schematic of domain structure in ferroelectric material (Fang et al. 2013)

Owing to the minimization of free energy, the crystal tends to decompose into domains with dipoles pointing to different energetically equivalent directions. The existence of domain wall energy prevents crystal decomposition from proceeding to the infinitely small domain

(single dipole). The formation of domains is a result of minimization of the sum of domain wall energy and electric field (Tichý et al. 2010).

5.1.2.2 Polling process and hysteresis loop

As mentioned above, the poly-crystal grains split into many domains owing to the requirement of energy minima. The directions of domains are random so that the net macroscopic polarization is zero. With the application of external electric field parallel or perpendicular to the thickness direction, the dipoles in the domains can be reoriented to align with the field direction, and the ferroelectric material could be brought into a polar state. This process is called the polling process.

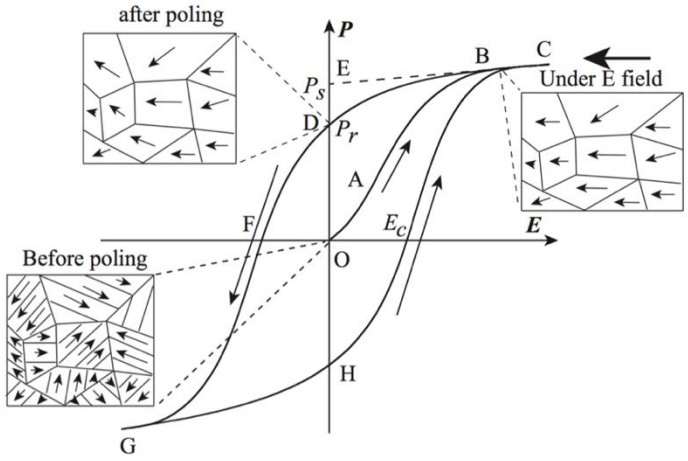

Figure 25. Typical hysteresis loop with domain structures before and after polling process. (Jin et al. 2014)

The behavior of polarization of ferroelectric material as a function of external electric field is non-linear resulting from the domain structure. Dielectric hysteresis occurs in alternating field. This behavior is shown in Figure 25 (Jin et al. 2014) and is known as a hysteresis loop,

which can serve as a proof of existence of ferroelectricity in the material. Decoding the hysteresis loop is thus an effective way to comprehend the ferroelectric property of the material.

Through the hysteresis loop, three important parameters can be determined: spontaneous polarization (P_s) , remnant polarization (P_r) and coercive field (E_c). At the origin, the domain structure before polling is sketched in the bottom left cubic in Figure 25. When the electric field is increased to high field (far right), the polarization is increased until saturation and then the material behaves as a linear dielectric. The saturation occurs as all the domains are oriented, which is shown in the upper right cubic of Figure 25. Extrapolating the linear segment to obtain the intercept with polarization-axis defines the spontaneous polarization (P_s). When the electric field starts to decrease, some dipoles are inclined to back-switch to original random state. But at the point where electric field is zero, the net polarization is nonzero due to the hysteresis, leading to the remnant polarization (P_r), for which the domain structure is shown in upper left cubic in Figure 25. To obtain a zero polarization, an opposite electric field is needed. Such field strength is called coercive field (E_c). When the opposite electric field continues to increase, the behavior of polarization is similar to the positive part.

5.1.2.3 Curie Temperature

The spontaneous polarization state remains in the ferroelectric material only in a certain temperature range. The crystal structure tends to be more symmetric with the increase of temperature, and will become a pure symmetric structure with little polarization, for which the state is called paraelectric. The temperature point where ferroelectric phase transforms to paraelectric is the Curie Temperature (T_c). Above the Curie temperature, the piezoelectric effect in the ferroelectric material is slashed drastically due to the loss of asymmetry and alignment of

dipoles resulting from the phase transformation. Thus, the Curie temperature is known as the upper limit of operating temperature range of the piezoelectric material.

5.2 PIEZOELECTRICITY IN POLYMER

Unlike crystalline materials, polymer units have length and molecular scales larger than atomic scale. The long chain molecular structure with one or more chemical motives repeating along the chain of polymer is totally different from the crystal unit cell structure of ceramics. And owing to extremely large number of conformations of the skeletal bonds of polymers in the space, the characterization of polymer chain is done only statistically. For preliminary understanding of the piezoelectric polymer, we classify the piezoelectric polymer as bulk polymer and cellular polymer.

5.2.1 Bulk polymer

5.2.1.1 Crystalline and semi-crystalline polymer

Crystalline polymer can be synthesized through special thermal processing, mechanical stretch and high voltage application on the polymer, where the distribution of molecular chains has long-range-order repeating patterns. The thermal history or synthesis method determines the degree of crystallinity of the polymer. For a polymer with relatively small fraction of crystalline volume, it can be classified as semi-crystalline polymer. Here we introduce the two prerequisites to get effective piezoelectric response out of the polymer, and the methods to achieve and enhance the piezoelectricity.

Similar to piezoelectric ceramic crystal principle, semi-crystalline polymers require charged molecule groups to form an electric displacement before they show the piezoelectric effect. But the production of dipole moments in polymers depends on not only the asymmetric structure of the molecule groups forming the dipole, but also on the arrangement of dipoles in the crystalline phase.

Poly(vinylidene fluoride) (PVDF) is one of the most commonly used piezoelectric polymers and can be used here to illustrate the operating principle of the above two factors. The electric dipoles of PVDF are formed owing to the C-F groups in the chain (shown in Figure 26) which exhibit polarization due to the large difference of electronegativity between the F atom and the C atom.

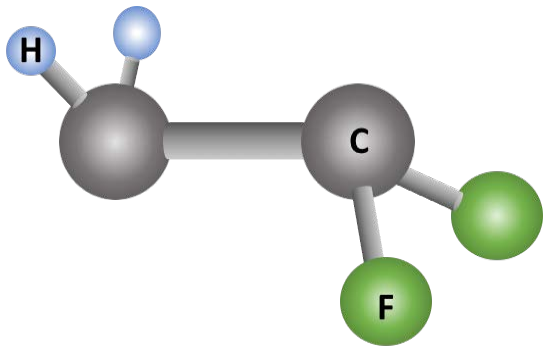

Figure 26. Molecular structure of the monomer of PVDF

Due to the stereo structure of the molecular chain and the variety of packing modes of the chain, there are at least 4 types of crystal structures of crystalline PVDF: α, β, γ and δ, which are presented in Figure 27(a) (Tashiro 1995). The single molecular chain in the α-structure PVDF has dipole moment along and perpendicular to the backbone, while the in the α-structure , the net dipole is zero, because of the antiparallel packing mode of the molecular chains (in Figure 27(b))

(Yu & Cebe 2009). Thus, the dipole moments of each molecular chain cancel out as shown as the dashed arrows in the bottom section of Figure 27(b), i.e. the α-structure crystalline PVDF is nonpolar.

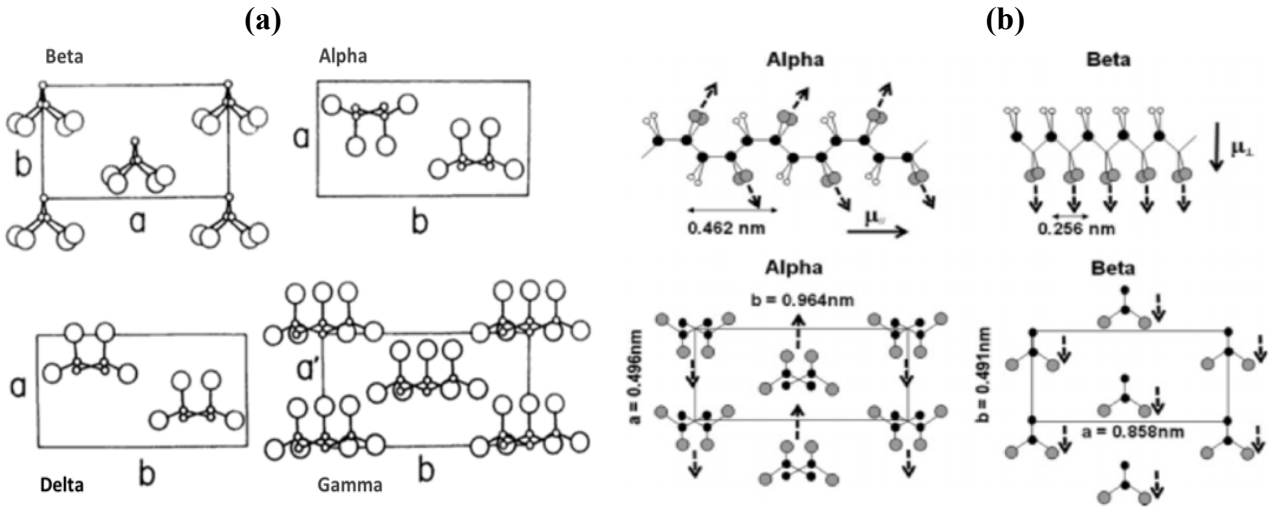

Figure 27. (a) 4 types of crystal structure modifications of PVDF (Tashiro 1995); (b) Evolution of $\boldsymbol{\alpha}$- and $\boldsymbol{\beta}$- crystalline from molecular chains of PVDF (Yu & Cebe 2009).

By analogy, the β-structure crystalline PVDF is, however, polar due to the parallel arrangement of molecular chains. And so are the γ and δ structure which can be obtained by slow-cooling the melt.

Normally these polar crystalline regions are randomly distributed in the semi-crystal polymer bulk. The schematic of the morphology of a bulk semi-crystal PVDF material is shown in Figure 28, where the polar crystallite regions are disorderly dispersed in the amorphous matrix. A permanent anisotropic arrangement can be achieved by mechanical stretching or electric polling, by which the crystallites can be reoriented to a preferable orientation.

The mechanical stretch method can be uniaxial and biaxial to align the amorphous strands and to facilitate the rotation of polar crystallites with the application of electric field. Electric polling of the polymer is commonly done by two methods: electrode polling and corona charge (Ramadan et al. 2014).

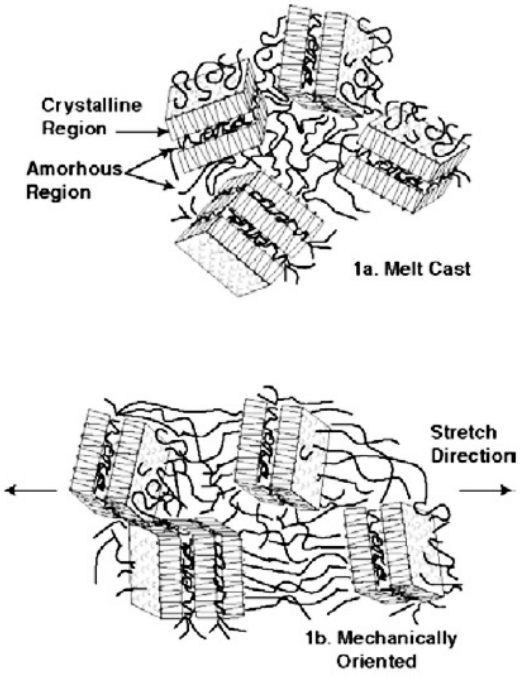

Figure 28. The schematic of the morphology of a bulk semi-crystal PVDF and after mechanical stretching. (Harrison & Ounaies 2001)

In the electrode polling method, the polymer is sandwiched by two polished metal plates under vacuum or immersed inside an insulating fluid (See Figure 29(a)). Usually an order of 5-100 MV/m (Dargaville et al. 2005; Wise et al. 2002; Li et al. 2008; Kim et al. 2011) DC electric field is applied across the two metal plates to effectively affect the crystalline orientation. Corona charge method is more complicated than the former one. It requires deposition of the electrode

on the surface of polymer film, and a higher voltage supply to achieve electrical arching. As shown in Figure 29(b), only one side of polymer film is connected to the electrode. On another side, there is a conductive needle subjected to very high voltage of about 8-20kV. Corona method is more advantageous in that the cover area of electrode can be small, and there is no need of hours of continuous polling time but only a few seconds are needed instead. This method is thus used as a part of the manufacturing method of commercial PVDF.

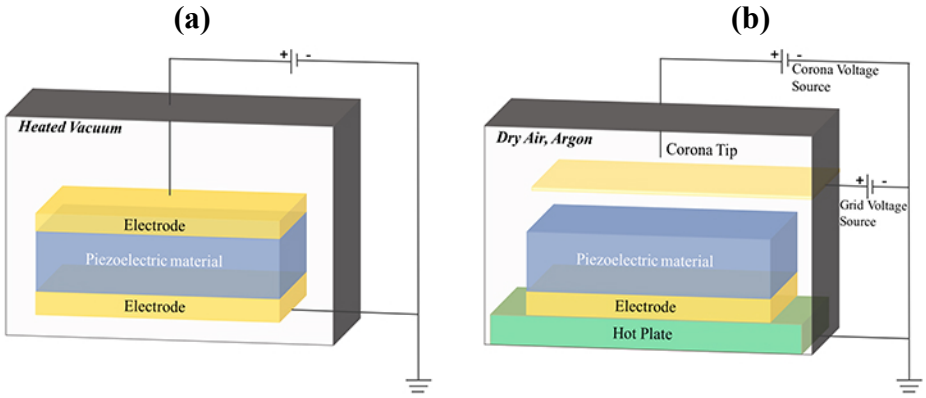

Figure 29. Two method of electrical polling: (a) electrode polling and (b) Corona polling**.** (Ramadan et al. 2014)

Other methods, such as electron beam polling and soft x-rays for ionization, that are less commonly used will not be covered in this thesis.

As a counterpart of the Curie temperature point in crystal ceramics, polymers have Glass Transition Temperature (Tg) as indication of polymeric phase transforming to glassy phase, where molecular chains are sufficiently mobile and decay of different properties of the material occurs. Tg thus serves as the upper limit of the operational temperature range of this kind of piezoelectric polymer.

Studies of piezoelectric polymer crystal materials have significantly increased recently. Other than PVDF, copolymers of polyvinylidene fluoride with trifluoroethylene (TrFE) and

tetrafluoroethylene (TFE) have also been found to exhibit strong piezoelectric effects for greater crystallization than pure PVDF. Polyamides and polyureas are also good alternative resources of piezoelectric (semi-)crystal polymer for the large net dipole moment of their crystalline structures (Kawai 1970; Newman et al. 1980; Takahashi et al. 1989). To further understand the relationship between modification of molecular structure of polymer and macroscopic piezoelectric property, a recent study reported the control mechanism of flexible ferroelectric polymer crystals (Owczarek et al. 2016).

5.2.1.2 Amorphous polymer

Commonly, the structure of polymers lacks long-rang order without crystallization processing, which renders most polymers as amorphous materials. In this section, we will explain how the piezoelectricity can be shown, and how to maximize the polarization and hence the piezoelectric response in amorphous polymers.

Unlike (semi-)crystalline polymers with polar long-range-order (crystalline) regions, amorphous polymers show piezoelectricity after certain processing of the polymer as long as the molecular chains contain dipole molecule groups.

In theory, the randomly dispersed molecular dipoles on the molecular chains can be aligned by an external electric field. However, the disordered structure of molecular chains and the solid state of polymer make dipoles hardly move when polling. Accounting that a maximum motion of molecular chains is achieved at the vicinity of Tg, an electrical field is applied when the polymer has been heated till the temperature is slightly higher than the glass transition temperature. Giving a glassy environment with minimum resistance of molecular chain motion, the molecular dipoles in the polymer are able to rotate under the instruction of electric field. After a certain amount of time for polling, the reoriented molecular dipoles are ‘frozen’ by

lowering the temperature to room temperature while still in the presence of the electric field. Therefore, quasi-stable polar regions consisting of reoriented dipoles can be formed, and they are the origin of piezoelectric-like property in the amorphous polymer.

The degree of polarization produced from this polling method can be derived from the Langevin equation in terms of the dipole moment, polling electric field and the temperature (Harrison & Ounaies 2001). The remnant polarization can then be related to both dielectric strength (HILCZER & MALECKI 1986; Harrison & Ounaies 2001) and piezoelectric coefficient (Mopsik & Broadhurst 1975; Bharti et al. 1995; Stefanou 1979) of the amorphous polymer. Therefore, to obtain the maximum remnant polarization, the optimization of (1) polling electric field, (2) dielectric relaxation time of the polymer and (3) polling temperature should be investigated.

Ideally, the larger the polling electric field that is applied, the higher the remnant polarization that can be formed. While in practice, the maximum polling field is limited by breakdown voltage of the polymer. A value of 100 MV/m is typically applied. The relaxation time of the material determines how long the polling time is supposed to be, which needs to be on the order of the relaxation time at that polling temperature. Since, at the vicinity of the glass transition temperature, remnant polarization of the polymer will not be maintained, Tg cannot serve as the upper limit of application temperature of such amorphous polymers, so the practical upper limit is well below the Tg.

5.2.2 Cellular polymer

Cellular polymers (also known as space charge electret) are the polymers that contain some amount of gas voids inside the bulk polymer. In this section, we explain the piezoelectric

mechanism of the cellular piezoelectric polymer, which are totally different from the bulk polymer, and briefly introduce the factors affect the piezoelectric response.

When the gas voids inside the cellular polymer are charged by Corona polling, a strong pseudo-piezoelectric property is exhibited. This electro-mechanical coupling property is regarded as pseudo-piezoelectricity, because the property is independent of the chemical aspect of the material, but only related to the porous structure of the polymer. Unlike bulk piezoelectric polymers, the piezoelectricity of cellular polymers is generated from the ionized gas in the voids, instead of molecular dipoles. The charged gas voids can be treated as dipoles for the space charges inside ionized gas. Space charges are attracted to concentrate on different ends of the void surface by the external electric field, and form the 'artificial' dipoles (See Figure 30). As a mechanical force is applied to the polymer, the deformation of voids cause a change of shape of the dipole and hence the dipole moments, so that the material outputs charges if it is connected with an electronic load.

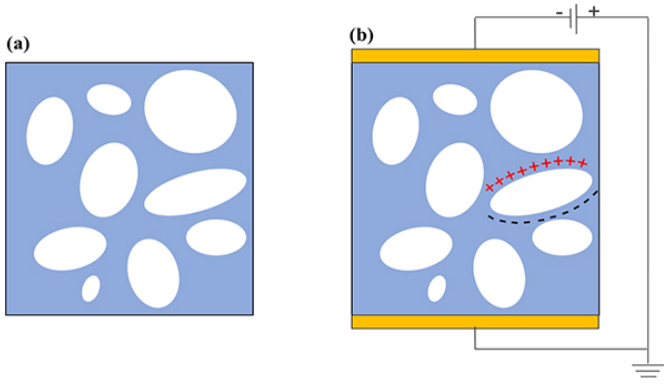

Figure 30. Illustration of piezoelectric cellular polymer: (a) schematic of the structure and (b) formation of gas dipoles after polling**.** (Ramadan et al. 2014)

Based on the space charge dipole structure, the piezoelectric response of the cellular polymer depends on the shape and density of the voids, which eventually determine the distribution of dipoles. Also, the type of gas inside the voids affects the degree of ionization, and hence the amount of space charges. Notably, another factor that influences the piezoelectric response is the frequency of input force/electric field, which causes no dominant change for regular piezoelectric materials. This can be accounted for by the slow resilience after deformation of the polymer, which is achieved by gas exhaust and entrance through voids. Therefore, the total displacement of the structure varies with different frequency of input. The piezocoefficient is required to be measured in both dynamic and quasi-static cases for accurately characterizing the piezoelectric response. Table 2 lists both the quasi-static and dynamic piezocoefficients of some typical cellular piezo-polymers.

Table 2. Piezocoefficients of typical cellular piezoelectric polymer

Name	Company	Quasi-static d_{33} (pC/N)	Dynamic d_{33} (pC/N)	Structure	Reference
HS-04	Emfit Corp	NA	250	Polymer & mineral void & electrode	(Anton & Farinholt 2012)
PTFE (HS-01) stretched	Emfit Corp	350	140	Cellular	(Hillenbrand & Sessler 2004)
PTFE (HS-01) un-stretched	Emfit Corp	200	130	Cellular	(Hillenbrand & Sessler 2004)
Multi-layer PTFE film	Self-process	2000	NA	Multi-layer sandwich	(Hillenbrand et al. 2002)
FEP	Teflon	100-280	NA	Sandwich	(Altafi et al. 2003)
EFoam	Expancel & self-process	330	NA	Sphere to bulk	(Windmill et al. 2008)

5.3 PIEZOELECTRICITY IN COMPOSITES

Combining the piezoelectric ceramics with high piezocoefficient and the polymer with excellent mechanical properties could potentially compensate for the drawbacks of each other. This motivation gave rise to the development of piezoelectric ceramic-polymer composites. Each component of the composite has their own contribution of piezoelectricity, so researchers can strengthen the piezoelectric response of the composite by choosing ceramics with high ion displacement and polymers consisting of large dipoles for the mechanisms mentioned in above sections. Other factors to be controlled to design the composite with desired features include: (1) connectivity patterns, (2) concentration of fillers, and (3) the size of fillers.

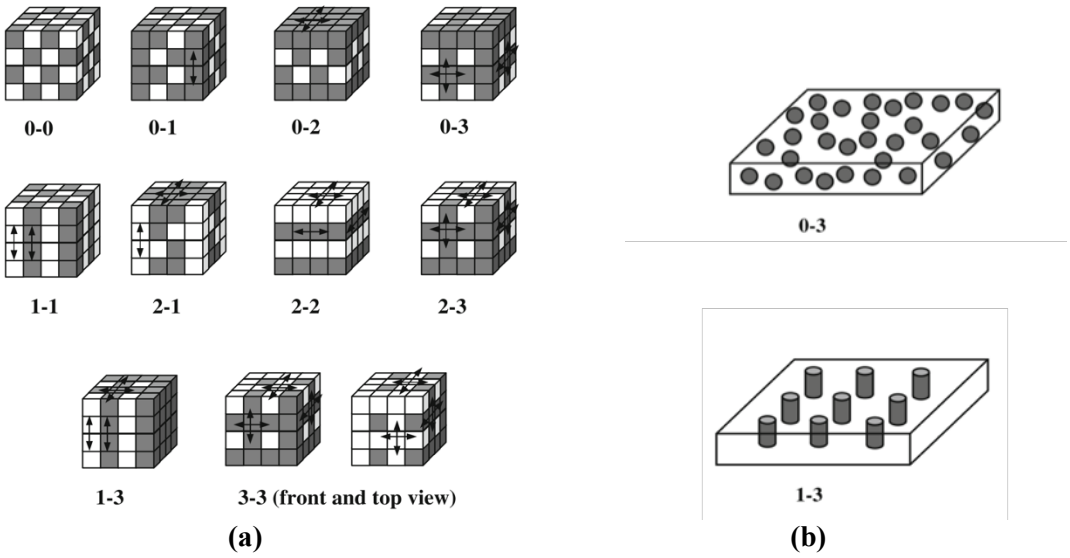

Figure 31. (a) Connectivity patterns and (b) piezoelectric composite with (0-3) and (1-3) connectivity. (Tichý et al. 2010)

The arrangement of ceramic-organic composites can have various combinations, which can be classified by different connectivity patterns (Newman et al. 1980). Figure 31(a) shows 10 types of connectivity patterns of two-phase (diphasic) composites, which are denoted by a 2-digit number showing the dimension of the ceramics (light color) and polymer (dark color). Dimension 0,1,2,3 usually refer to the structure of particles, rods, layers, matrix, respectively. Most common patterns for millimeter or micrometer scale devices include (0-3) and (1-3) modes (See Figure 31(b)).

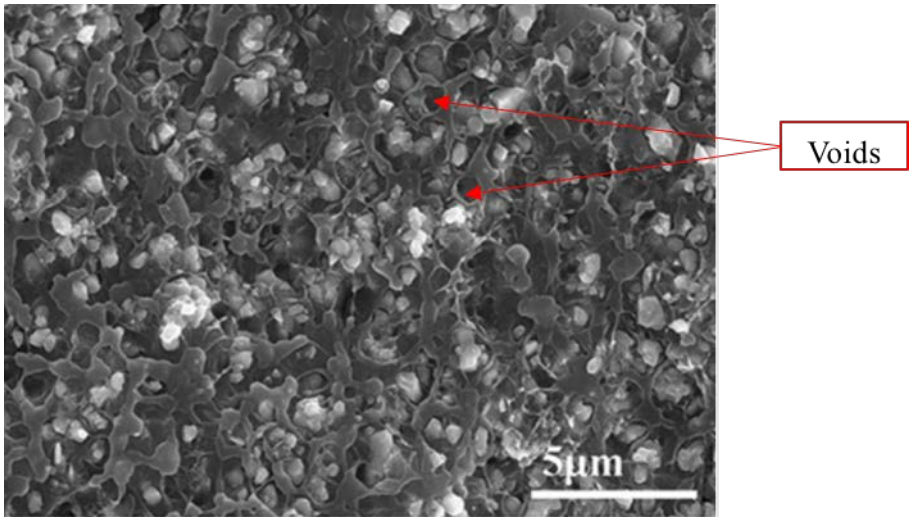

Figure 32. Scanning electron microscopy image of the cross-section composite with FTN ceramic and PVDF. (Fu, Hou, Wei, et al. 2015)

In the composite with (0-3) connectivity, ceramic powders are dispersed inside a 3-dimentionally connected polymer matrix. The fabrication process of this connectivity pattern is simple, but special care should be taken to achieve uniformly dispersed fillers. From the scanning electron microscopy image (see Figure 32) of the cross section a (0-3) composite with 40 vol% $FeTiNbO_3$ (FTN) ceramic as the fillers and PVDF as the matrix, it is obvious that this

connectivity induces gas voids within ceramics particles and between the interface of PVDF and FTN (Fu, Hou, Wei, et al. 2015). The presence of voids is the biggest limiting factor for high piezoelectric property. Since it dramatically reduces the dielectric breakdown voltage of the composite, rendering polling to full saturation is virtually impossible.

In the (1-3) connectivity pattern, ceramic rods are scattered in polymer bulk. Since the ceramic is far harder than the compliant polymer phase, one of the advantages of this rod structure is that the applied stress can be transferred more efficiently, which increases the g_{nij} piezocoefficient of the composite. However, this case sometimes may be weakened when the internal stress is opposite to the external applied stress, where the amplification of stress is reduced due to the high Poisson's ratio of the polymer (Haun 1983).

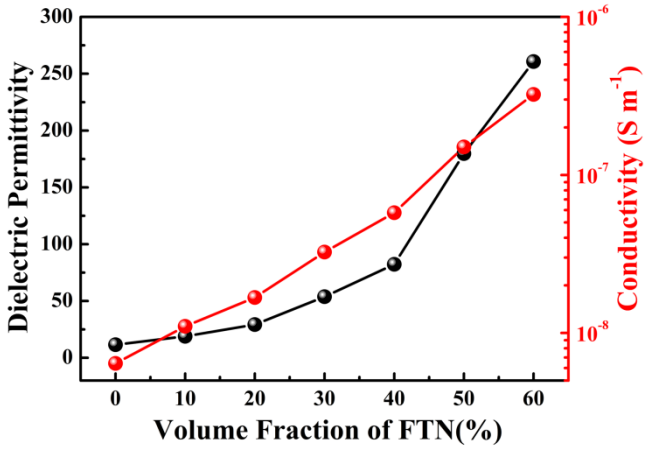

Figure 33. Variation of dielectric permittivity and conductivity of the FTN-PVDF composites as a function of different volume percentage of FTN at 25℃, 100Hz. (Fu, Hou, Wei, et al. 2015)

The piezoelectric behavior of the composite is strongly dependent on the concentration of the fillers, due to the huge difference in the magnitude of polarization between the fillers and matrix. Figure 33 shows a sharp increase in the electric property of the (0-3) composite with the

volume percentage of FTN ceramics increase. This results in an unstable piezoelectric property of the composite when the concentration of the filler is hard to control precisely.

The effect of the filler size on piezoelectric and dielectric property has been studied by many researchers (Fu, Hou, Zheng, et al. 2015; Lee et al. 1986; Lee et al. 1988). It was found that in (0-3) PT-PVDF composite, the d_{33} constant decreased with the reduction of PT size, while the larger the ceramic size, the worse the mechanical flexibility.

Based on the variety of studies of the factors affecting the piezoelectric properties of composites, it is essential that balancing for both pros and cons of the material type, connectivity patterns, and size and concentration of the fillers is important in order to design a material system for a specific application with desired properties.

5.4 ADOPTED MATERIALS

After reviewing most of current piezoelectric configurations and materials, the cellular polymers in section 5.2.2 and the THUNDER configuration with ceramic thin film mentioned in 3.1.3 are featured by their flexibility, which are thus adopted in this thesis research for the SMSH application.

5.4.1 Doped polyurethane foam

Inspired by the gas cellular structure of extreme flexible polymers, and the polarization induction concept of polar nonlinear optical (NLO) compound materials, our collaborating group (Moody et al. 2016) developed a flexible doped polyurethane foam with competitive

piezoelectric coefficient value of 244 pC/N (See Figure 34). The concept of polarization induction into NLO is that doping a non-polar polymer with another polymer that has high dipole moment, can yield success in improving the piezoelectric response in this composite polymer (Shi et al. 2000; Ma et al. 2002). Since normal polyurethane foam has little piezoelectricity but high flexibility, the doped highly polar molecules are dispersed in a nonpolar polymer matrix and poled to produce axial alignment which enhances the piezo-response of the whole polymer system.

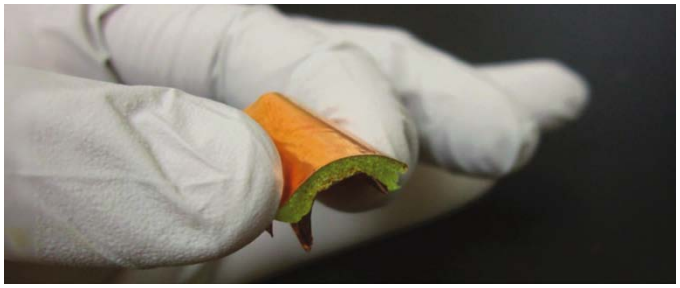

Figure 34. Demonstration of flexibility of doped polyurethane foam sample.

Similar to amorphous bulk polymer mentioned in 5.2.1, the piezoelectricity in the foam is dependent on the dipole moment of the molecular groups and the anisotropic degree that the dipoles can achieve. In this material, it is theorized that molecular dipoles and matrix are from two separate polymers: here, 2-chloro-4-nitroaniline as the dipole, and polyurethane as the matrix. Two parts of liquid precursors was mixed to synthesize the polyurethane, and then the mixture cures and forms the cellular polymer matrix. Instead of heating the matrix to a glassy state, the liquid state of the mixture was taken advantage of to ensure enough motion of dipoles, and the polling process is applied as the polymer is curing. The details of procedures of this method will be covered in Chapter 6.

This dopant approach has a considerable advantage in the polling process. Through the analysis in the last section, the drawbacks of current permanent polarization induction methods for polymers can be seen: such as the long-time heating when polling, or the extremely high power requirement for the Corona charge. In addition, this approach does not require heating of the sample to the glass transition temperature.

5.4.2 THUNDER-type PZT thin film

Another noticeable material that can be largely deformed is the THUNDER-type PZT thin film, which was already introduced in section 3.1.4. Different from soft doped polyurethane foam, the flexibility of the THUNDER is from the ductility of the electrode metals and the elasticity of the dome structure (See Figure 35). The dome height determines the maximum deformation that the device can achieve. It can be as high as 10 mm for this model, which satisfies the requirements of SMSH application very well.

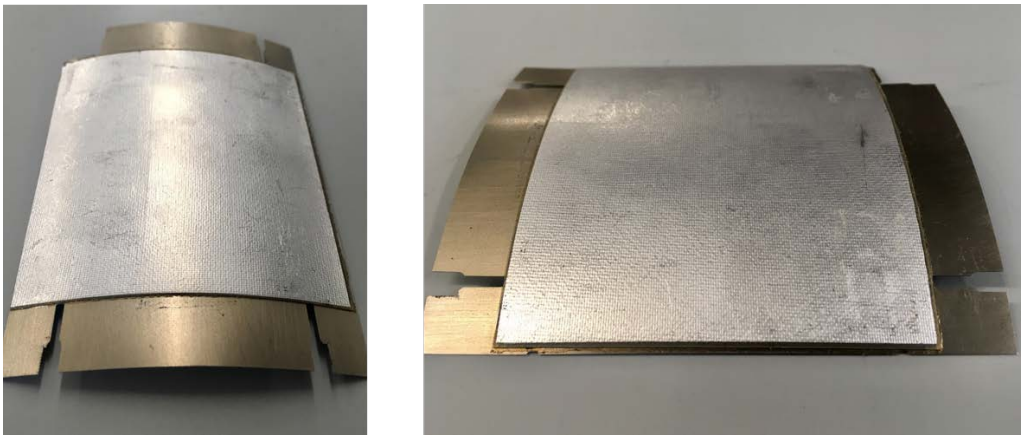

Figure 35. Photo of THUNDER-type PZT thin film actuator (TH-7R).

In this thesis, the TH-7R model of the THUNDER actuator from the Face Company was also adopted for the experimental part. The specification is summarized in Table 3

Table 3. THUNDER specifications

Name	Dimension L×W×H (inches)	Weight (grams)	Dome Height (inches)	Capacitance (nF)	Resonant Frequency (Hz) (simply support)
TH-7R	3.8×2.8×0.023	18.0	0.377	166	106

6.0 EXPERIMENTS

6.1 SYNTHESIS OF PIEZOELECTRIC FOAM

Two parts of liquid precursors (PolyFoam-F-3) of polyurethane were prepared from Polytek Development Corporation: Part A is yellow liquid Methylene bis(phenyl isocyanate), and Part B is extremely viscous white liquid Polyther polyol. 2-chloro-4-nitroaniline (98%CNA) as dopant was obtained from Tokyo Chemical Industry Co.Ltd. The whole process of synthesis consists of three steps: (1) Doping; (2) Mixing two parts of precursors; (3) Polling and curing the foam, (Moody et al. 2016) which are shown in Figure 36.

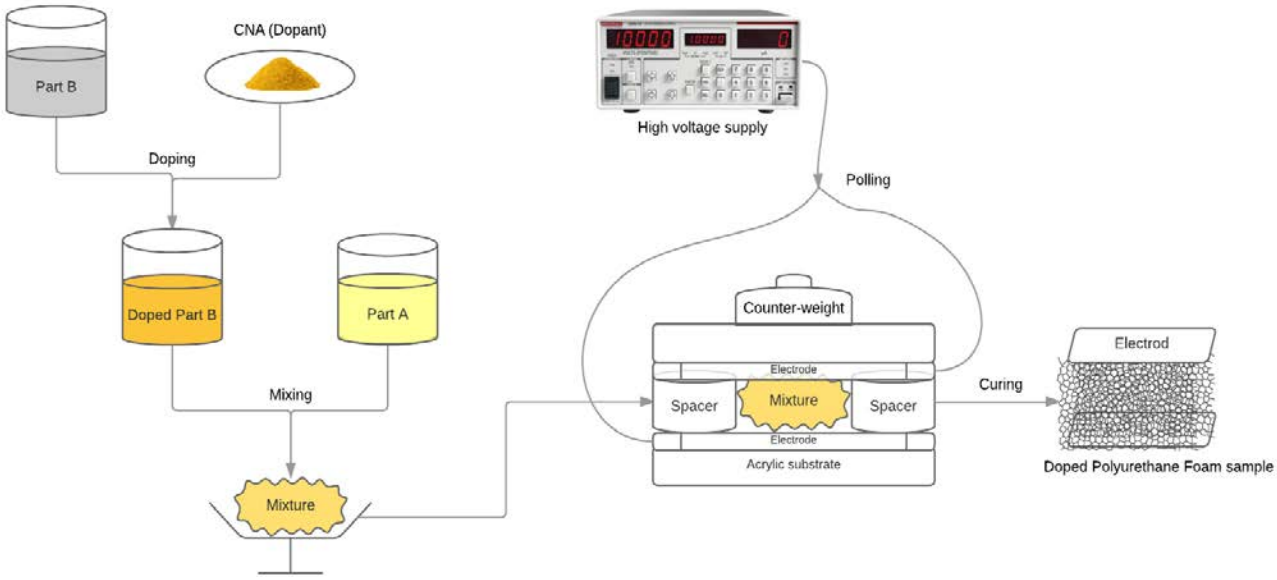

Figure 36. Process of synthesis of piezoelectric doped foam sample.

In the first step, the CNA powders were dispersed only into Part B of the precursors. Knowing the molecular weight of CNA is 172.568 g/mol, the concentration of the dopant was controlled to be 0.1 mol per Liter solvent (0.1 M/L). Due to the extremely viscous nature of Part B, CNA powders were dissolved by means of ultrasonic vibration, or in 40℃ water bath if necessary. The doped Part B then was allowed to sit statically for 2 days to ensure that the dopant was uniformly dispersed.

In the second step, the weights of Part A and Part B were measured and controlled. The mass ratio of Part A and Part B determines the degree of softness of the polymer. The weight of dopant was neglected due to the small concentration. A ratio of 1:2 was used for mixing. Either a mechanical stirring device or a glass rod by hand can be used to mix the two parts. During the mixing, the reaction of Part A and B is exothermic, and thus the reaction rate depends on the quantity of the reactors. For about 0.5 grams Part B, a mixing time of 30 seconds was adopted. After mixing, a 0.2 mol/L solution of two parts of precursor were obtained.

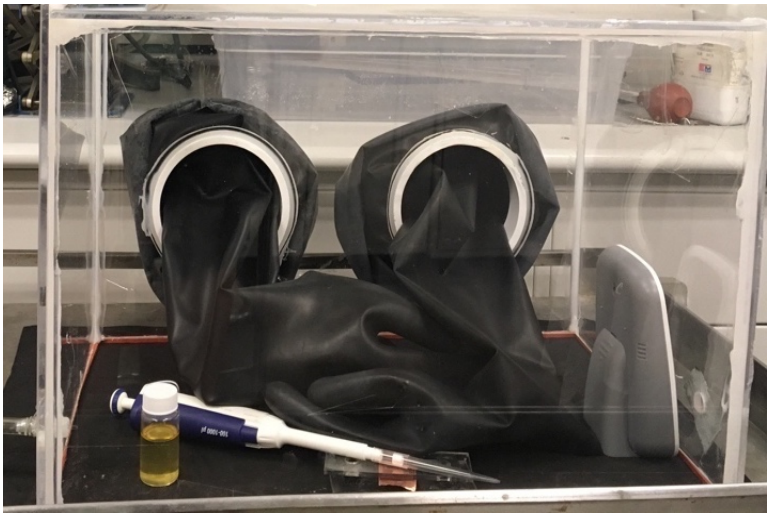

Figure 37. Photo of humidity control operation box

This step is a water-sensitive step. The humidity should be controlled to be below 20 RH% using an operation box full with nitrogen gas as shown in Figure 37.

In the third step, the viscous liquid mixture should be rapidly placed onto the copper foil, and then be covered by another copper foil supported by two plastic spacers (See Figure 36). The spacers set the final thickness of the specimen. The copper foils serve as electrodes. A voltage bias of up to 2kV was applied during curing. Because of the expansion of the curing foam, a counterweight was placed on the top of this sandwich structure. The periphery of foam was left open to allow for expansion of the foam. The product of CO_2 was released to the air during curing, which formed the gas voids inside the material. The electric polling field was removed after the foam was fully cured, which took about 120 ~ 160 minutes.

6.2 MEASUREMENTS OF PIEZOELECTRIC PROPERTY

6.2.1 Measurement of quasi-static and dynamic piezoelectric coefficient

In this section, the discussed measurements of piezoelectric coefficients are all based on direct piezoelectric effect. The sample was evenly loaded with an excitation force F, and then the current generated by the piezoelectric sample due to the change of load was measured. The measured current can be expressed as:

$$i = d_{ij}\frac{dF_i}{dt} \tag{6-1}$$

The generated charge is hence:

$$Q = \int_0^t i\,dt = d_{ij}\int_0^{F_i} dF_i = d_{ij}F_i \tag{6-2}$$

So, the piezoelectric coefficient d_{ij} can be calculated from the slope of Charge-Force plot.

The difference between quasi-static and dynamic coefficients is the frequency of excitation force when they were measured. Normally, for most piezoelectric materials, there is no obvious difference between their quasi-static and dynamic coefficients. While for largely-deformed piezoelectric foam/dome, the dynamic piezo-coefficient is lower than the quasi-static one, due to their slow resilience which was mentioned in 5.2.2.

To obtain the quasi-static direct d_{33}-costant, cycles of press-release excitation with frequency less than 10 Hz was applied by hand on the sample with two electrodes. The value of pressure varied with each cycle, and was recorded by a force sensor, while the current generated from the sample was measured and recorded by sensitive source-meter.

The charge data from about 12 cycles of excitation was grouped and plotted as a function of force applied. Linear regression was used to get the value of the slope of the function, which is the value of the quasi-static d_{33}-constant. Values of d_{33} from 3 groups are averaged to minimize errors.

It should be mentioned that the d_{33} constant of the foam is also pressure dependent. If the foam is about 80% deformed, the displacement is non-linear to the applied force and thus will affect the piezoelectric response to the mechanical input.

To obtain the dynamic direct d_{33}-constant, the frequency of excitation range from 10 Hz to 1kHz was carried out. Unlike the previews method, the sample with two electrodes of area A was sandwiched by a mass M on the top, and a shaker at the bottom. As the shaker oscillated sinusoidally, two forces were loaded on the sample:

$$F_M = M \cdot g = P_M \cdot A, \qquad F_a = M \cdot a = P_a \cdot A \tag{6-3}$$

where g is gravity acceleration and a is the shaker acceleration, P_M and P_a are the pressure resulting from F_M and F_a , respectively. Here, the generated current corresponds to effective total force instead of the quasi-static load mentioned in last method.

6.2.2 Measurement setup for quasi-static piezoelectric coefficient

Considering our SMSH application aims to harvest energy of which the main source is from low-frequency human movement, we only investigated the quasi-static to low frequency piezoelectric constant of the sample in this article.

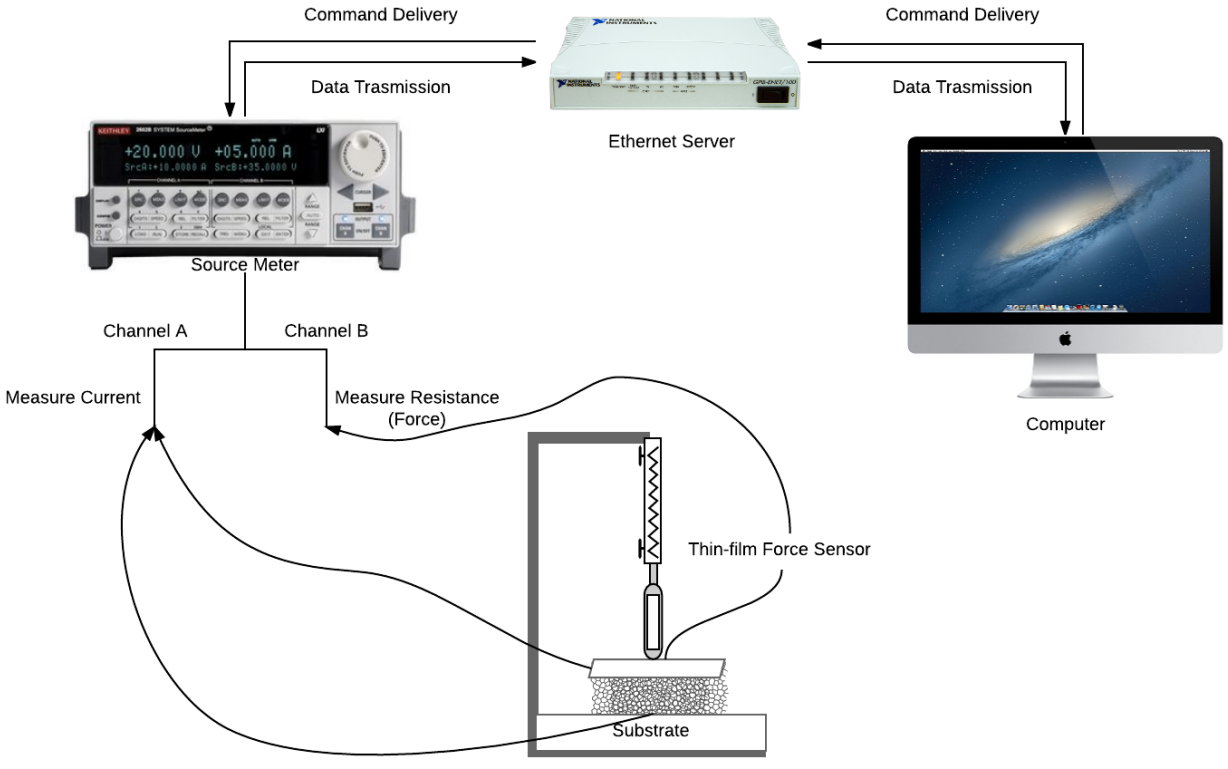

Figure 38. Schematic of measurement setup of quasi-static d_{33} coefficient.

The whole measurement setup consists of four main parts (shown in Figure 38): Computer; Ethernet server 'GPIB-ENET/100' from National Instruments; 2600 series Source-Meter from Keithley; and sample operation platform, of which the resistive force sensor is from FlexiForce™.

The Source Meter is also known as source-measurement-unit. It is the combination of either a current source with voltmeter in parallel (Mode 1) or a voltage source with ammeter in series (Mode 2). Source and measurement cannot be separated. For measuring resistance, both modes work well as shown in Figure 39 and serve as an ohmmeter. For measuring current, Mode 2 was used and the voltage source was set to be 0 V, therefore the Source Meter acts as an Ammeter.

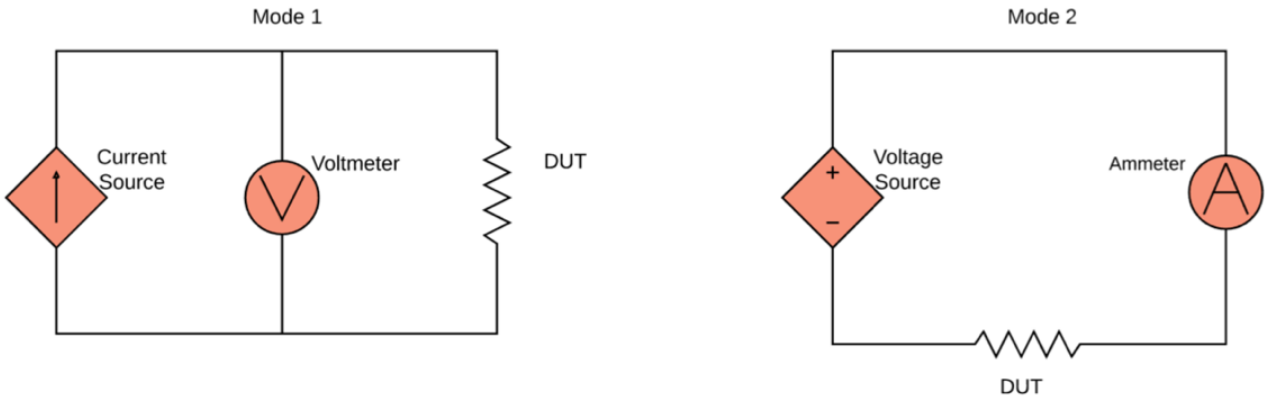

Figure 39. Two modes of sourcing and measuring in the Source Meter

To collect the measurement data, a customized application on the computer was programmed to 'talk' to the Source Meter through the Ethernet server. Channel A of the Source meter was assigned to Ammeter Mode for measuring the short-circuit current generated from the piezoelectric sample. Simultaneously, Channel B was assigned to Ohm-meter to measure the

resistance change of the thin-film force sensor. The effective circle area of the force sensor was placed right under the plastic rod that is used to apply pressure to the sample (See Figure 40). All the data from these two channels in time domain were transmitted to the computer via Ethernet. The sampling rate of the data collection is about 29.3 Hz ($\Delta t \approx 0.0341\ s$).

The raw data was then processed on the computer. As mentioned in the previous section, data of current from Channel A was integrated over time to obtain the value of charge. The resistance data from channel B was transformed into the value of force on the specimen based on the equations provided by the datasheet of the force sensor. After calculating the values of both charge and force, we were able the extract the quasi-static d_{33} coefficient from the slope of Charge-Force plot.

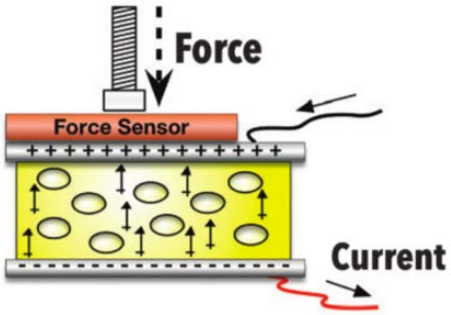

Figure 40. Sketch of placement of force sensor and sample subjecting force produced by a screw rod. (Moody et al. 2016)

It should be mentioned that the resolution of the Source Meter is high enough ($\sim 1 \times 10^{-8}$A) to avoid the need of a charge amplifier, which is typically an indispensable part of traditional measurement setups for piezoelectric coefficients because the magnitude of current generated from the piezoelectric samples is on the order of Pico-Amps.

6.3 INTERFACE CIRCUITS AND TEST RIG

6.3.1 Building interface circuits

All the resistors, wires and breadboard of the interface circuits are from Digi-Key Electronics. The diodes for building the rectifier are unidirectional 1.5KE-100A-9745 Transient Voltage Suppressor (TVS) diodes, considering a potential high voltage (~ 60V) may appear on the interface circuit when measuring the output power with varying resistive load.

A unidirectional TVS, like any other avalanche diode, operates as a rectifier in the forward direction, but is designed and tested to handle large peak currents. A higher power output may be obtained if Schottky diodes are used, of which the forward voltage (1.2V) is smaller than TVS (3.3V). However, for the purpose of proving the concept of SMSH, where current surges will frequently appear as the switch is connected to short the piezoelectric element, a TVS diode is a better choice in our application.

6.3.2 Test rig for measuring output power

There are three main parts of the test rig for measuring output power as shown in Figure 41: (1) excitation control part, (2) piezoelectric harvester system, and (3) output display part.

The first part is used to provide a mechanical input, for example to mimic a human footstep. The shaker LDS V201 from Ling Dynamic System provides the excitation on the piezoelectric element, and is controlled by an AC power input. The AC power is produced by an Agilent Function Generator 33220A amplified by an Operational Amplifier OPA512 from Burr Brown, which is charged by a DC power supply. The shaker was mounted upside down to an

aluminum frame. A flat-head screw drilled into a metal thin block is installed into the shaking tip of the shaker, which has the same thread as the screw. This flat-head screw is kept contact with the piezoelectric material for applying and releasing force at a certain frequency. A low-profile thumb nut is used to fasten the screw so that the distance from the metal thin block to the piezoelectric element can be controlled.

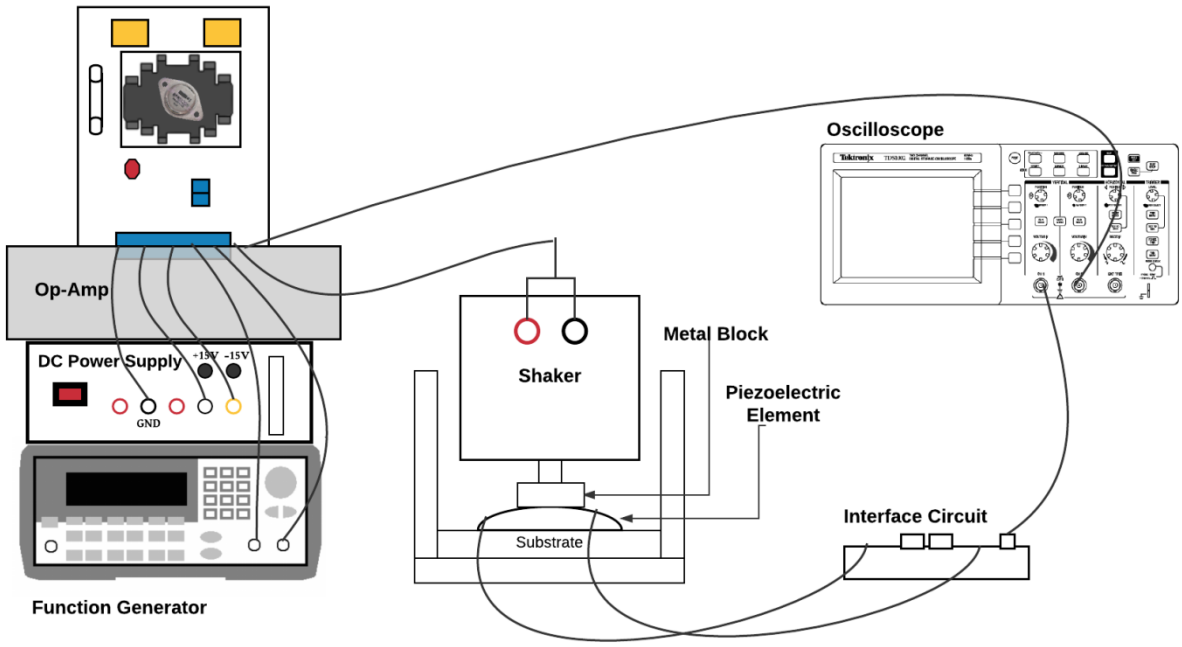

Figure 41. Sketch of test rig for measuring output power of piezoelectric harvester.

In the second part, the THUNDER is supported by the base of the shaker, and is pre-loaded by the compression of the shaker which is mounted upside down. The pre-loaded deflection is larger than the vibration magnitude, which ensures the contact between the shaker and THUNDER during motion. The interface circuit built on a breadboard is connected with the output of the THUNDER. The two thimbles of a micrometer are used to build the mechanical

switch. They are covered by copper foil and are connected to each other. As shown in Figure 42, a wire connects the thimbles with the superstrate electrode of the THUNDER, meanwhile the substrate of the THUNDER is placed between the two thimbles of the micrometer. When the THUNDER was deformed by the shaker motion, the substrate electrode hits the thimble at the maximum and minimum of the displacement, corresponding to the positions of the upper and lower thimble, respectively. Hence the THUNDER would be grounded as it hits the thimble, which works as the mechanical switch.

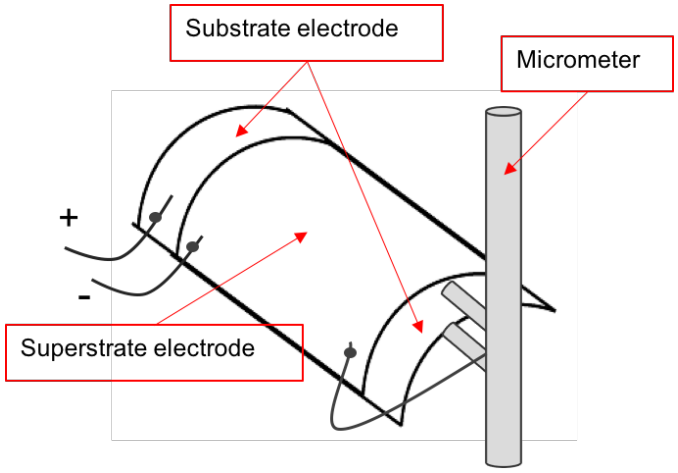

Figure 42. Configuration of SMSH using micrometer

In the third part, the output voltage of the resistor load on the circuit board is detected and recorded by a Tektronix-TDS 2014B digital storage oscilloscope. Meanwhile, the output of the Op-Amp in the first part is also monitored by the oscilloscope, which is known as the input voltage to the shaker.

The output power is calculated based on the load voltage V_L of the THUNDER, which can by expressed as:

$$P = \frac{1}{T}\int_0^T \frac{V_L^2}{R_L}\,dt \tag{6-4}$$

where T is the period of the load voltage, R_L is the resistance of the load.

The SMSH and measurement setup of output power is presented in Figure 43. Additionally, it should be mentioned that, based on the manual of LDS V201 shaker, useful frequency range for shaker vibration is between 5 to 13,000Hz (the upper frequency is bounded by the resonant frequency of the shaker's armature). This operating range is reduced significantly by the structure's dynamics, but it can be assumed that the phase difference between input voltage of shaker and the deformation of the shaker is negligible at low frequencies, and thereby the input voltage signal can be used to represent the displacement of the shaker and the THUNDER, since it's proportional to the input voltage of the shaker.

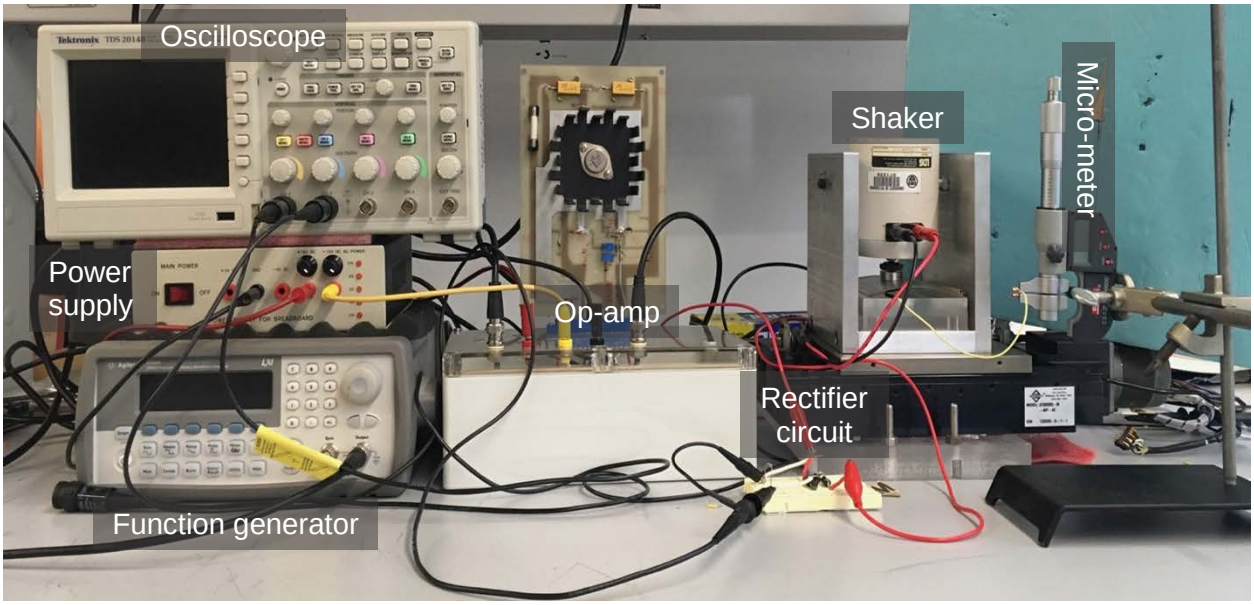

Figure 43. Photo of SMSH and measurement setup of output power

7.0 RESULTS AND DISCUSSION

7.1 QUASI-STATIC PIEZOELECTRIC COEFFICIENT

In this section, the measurement results of the quasi-static d_{33} of doped piezoelectric polyurethane are presented. Before starting the measurement, a verification of the accuracy of the test rig for measuring quasi-static piezoelectric coefficient was done: the piezo-constant of a commercial PVDF (DT4-052K) from Measurement Specialties Company was measured using our test rig and was compared to the corresponding parameter from its data sheet.

Figure 44 shows three results of charge generated (orange lines) from PVDF as it was subjected to a variety of pulse forces (purple lines). In Figure 44 (a), the relatively high values of forces were used to compress the PVDF sample (33 mode). The noisier signal between two charge peaks than the ones in Figure 44 (b) and (c) are due to the fact that more friction between the glass plate and the sample was produced as larger amounts of pressure were applied and released in (a). From Figure 44 (a), (b) and (c), it can be seen that the baseline of generated charge drifted downward as more and more force pulses were applied. This is because there is negative initial current in the channel ranging from 0.5 to 5 pico-Amp. Usually, this amount of background noise would not affect the measurement results. While the charge generated from piezoelectric materials is on the order of pico-Coulomb scale, the background current noise causing a drift of charge could be obviously seen in our results. However, when determining the

piezo-constant of the material, we use the ratio of the change of force value and the change of the charge value instead of the peak value of the charge, where the change of value is found by subtracting the bottom value from the peak value for any pulse. Therefore, the drift background is canceled and has little effect on obtaining the accurate value of piezoelectric coefficient of the material.

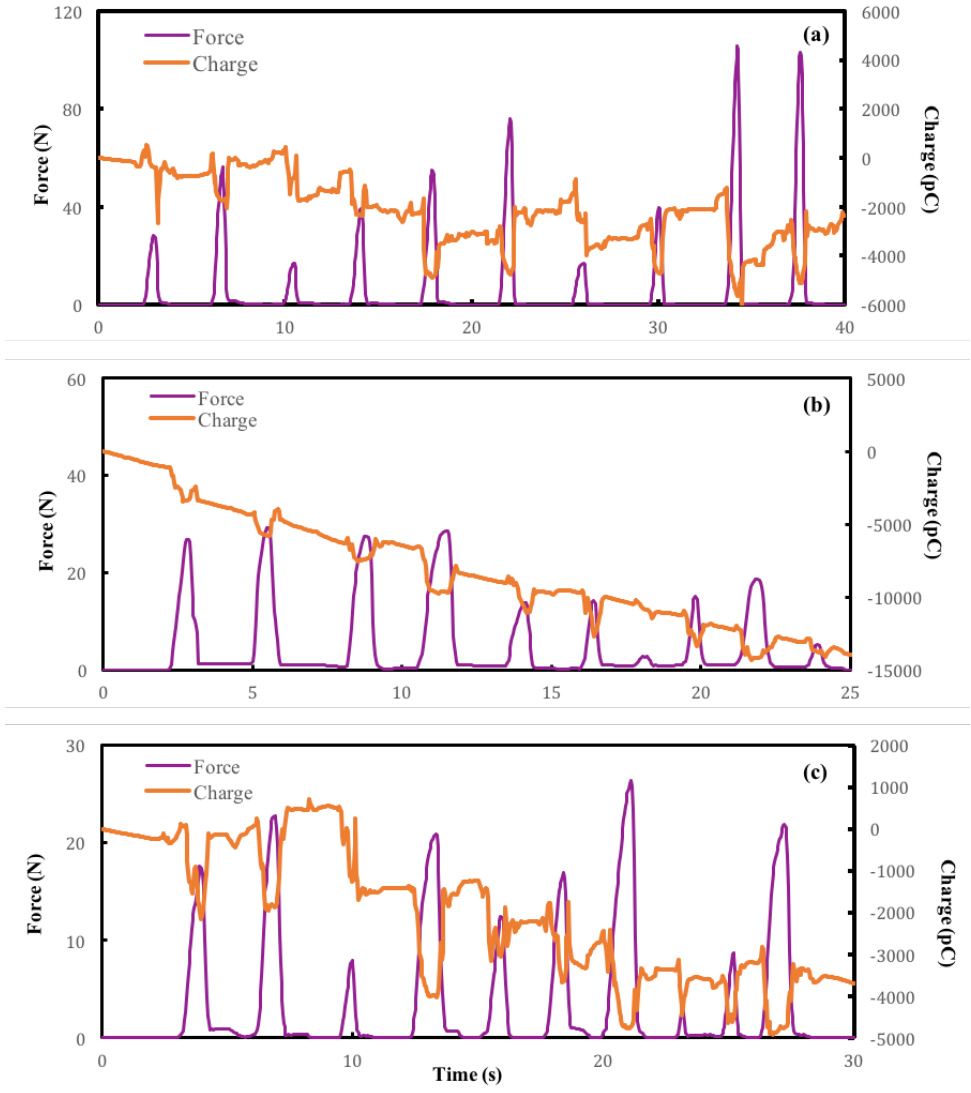

Figure 44. Three groups of piezoelectric response of PVDF within different force range.

Three values of piezoelectric constant of the PVDF were then calculated based on these three groups of data. Both d_{33} results and the R-squared of the linear regression in each group of data are shown in Table 4.

Table 4. Experiment results of piezoelectric constant d_{33} measurement of PVDF.

	Trial 1	*Trial 2*	*Trial 3*
d_{33} (pC/N)	-36	-38	-33
Reference d_{33} (pC/N)	-33 (TE_Sensor_Solutions 2015)		
R squared	0.84	0.24	0.62
Error (%)	6%	15%	0%

A value of 35.5 ± 2.5 pC/N for d_{33} of PVDF was obtained, which is in agreement with the reference d_{33} from the datasheet (TE_Sensor_Solutions 2015). It should be mentioned that one group of data has the largest error (Trial 2), and as such a poor R squared was obtained, which can be regarded as an indicator of the accuracy of the result based on the corresponding data group.

A negative number of the d_{33} means that negative current was produced as the sample was compressed by a positive force, and a positive current was produced when the force was released from the material.

After verifying the reliability of the measurement equipment, the piezoelectric coefficient of a 0.1mol/L CNA piezo-foam poled by a 400 V/mm field was measured. Figure 45(a), (c) and (e) are the three groups of measurement results showing the short-circuit current (gray lines) and

charge (orange lines) generated from the doped polyurethane foam with application of force (purple lines) at random frequencies. Then the d_{33} constant was calculated as the regression slope of Force-Charge plot. Figure 45(b) shows the linear regression result from (a), and (d), (f) are corresponding to (c), (e) respectively.

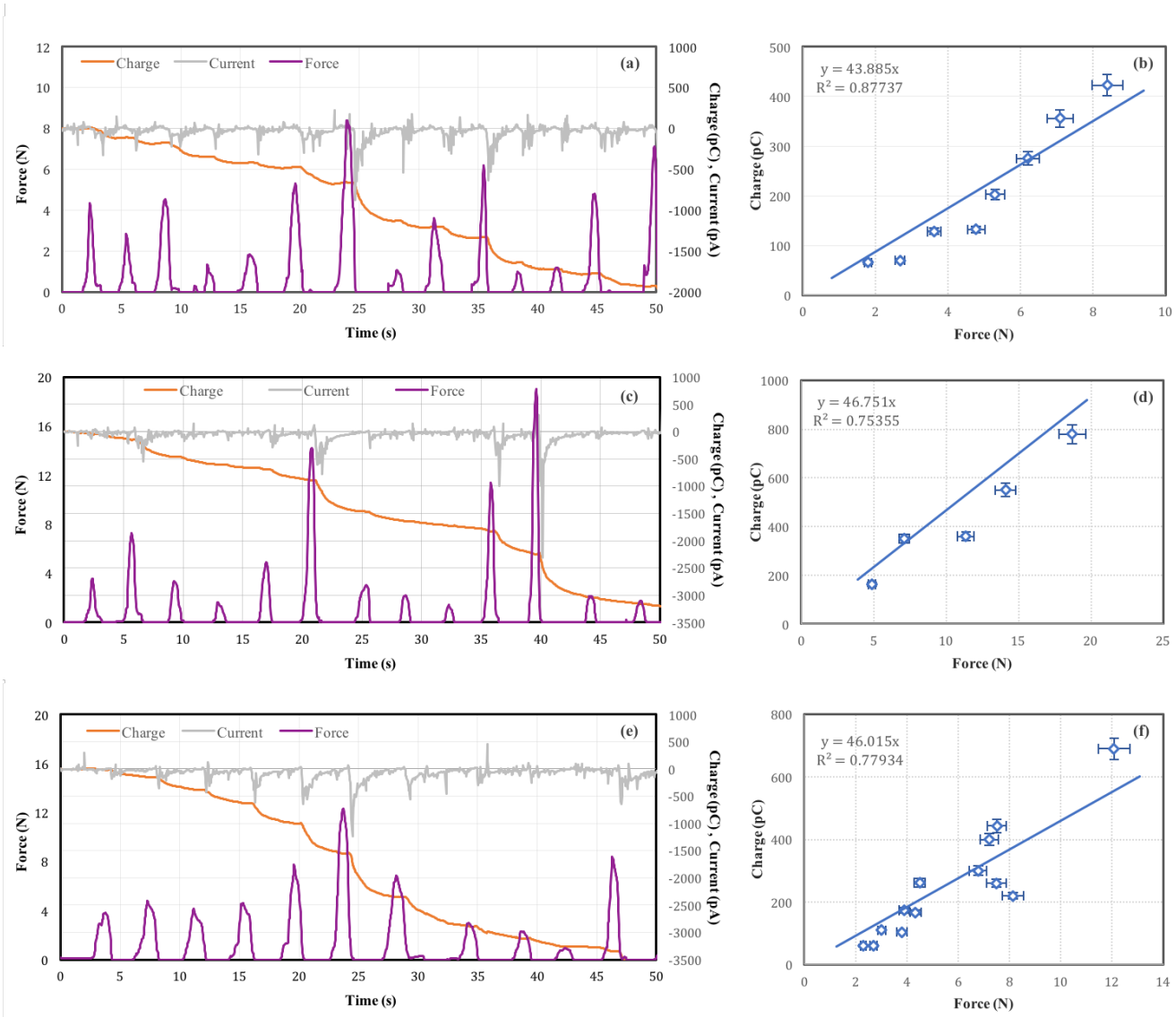

Figure 45. Piezoelectric response of piezo-polyurethane foam in (a) (c) (e) and the linear regression for obtaining the d_{33} in (b) (d) (e)

Based on the short-circuit current curve in the piezo-response plots, there is only negative current that was examined, and only a few large positive current pulses were recorded. Thus, the charge generated was no longer a peak but an abrupt drop right after the force was released. The amount of the drop was considered as the change of the charge produced by the foam, which is strongly proportional to the force applied, resulting in high R squared values of the force-charge linear regression models (Shown in Figure 45 (b), (d), (e)).

A value of 45.32 ± 1.43 pC/N of d_{33} was obtained from the piezoelectric response of the doped polyurethane foam, which is higher than that of PVDF. One possible reason to explain the higher piezo-response of the foam is that the polarization change in compression process is due to the change of material volume (Moody et al. 2016). Owing to the existence of gas in foam structure and a lower Young's Modulus, the piezo-foam can produce larger volume change with the same amount of force applied. Thus, assuming the total polarization of the two materials is comparable, a larger polarization change can be produced in the foam than in PVDF under the same amount of pressure applied, resulting in a larger piezo-coefficient of the doped polyurethane foam. An estimation of the d_{33} constant as a function of Young's Modulus of the foam and the dipole moment of the dopant CNA was calculated, which was predicted to achieve as high as 140 pC/N for a 0.5 mol/L CNA doped polyurethane (Moody et al. 2016).

In a normal piezoelectric element, current is generated as force is applied, and when the force is released from the material, the current is discharged in the opposite direction, so that the piezo-material performs as an AC power source. However, in the doped piezo-foam, a pseudo-diode property was found, where only one-direction current was allowed to flow in the short circuit as shown in Figure 45. The piezo-response of another foam sample with this property but subjecting heavier pressure is shown in Figure 46 (a). When the applied force was larger than

about 50 N, an abrupt huge positive current peak was generated, for which the peak value was proportional to the amount of force. To exhibit this pseudo-diode piezoelectric response of the foam, the enlargement of the green box in Figure 46 (a) is presented in Figure 46 (b). It should be mentioned that, after changing the polarity of the electrodes attached to the sample, both directions of current were generated (shown in Figure 46 (b) and (c)). This result provided further evidence of the possibility that asymmetric conductance exists in the doped piezo-polyurethane foam.

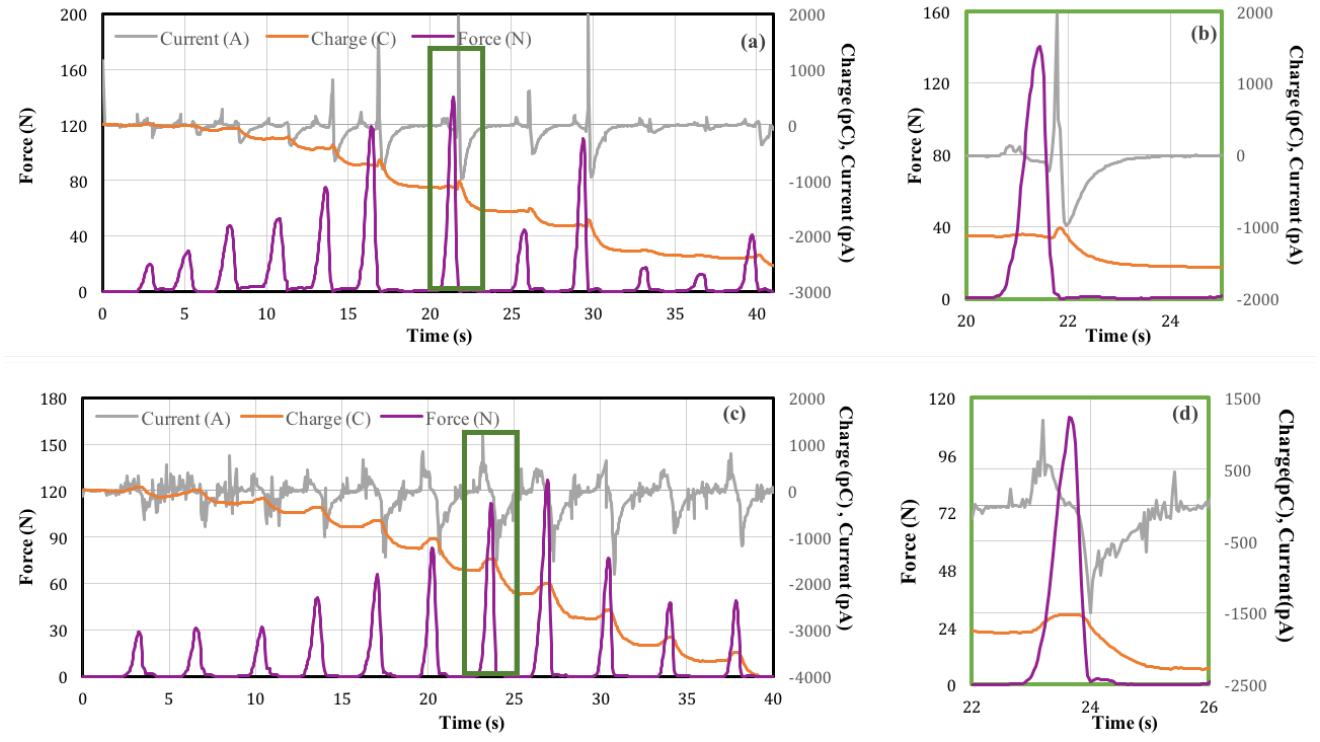

Figure 46. Piezoelectric response of piezo-polyurethane foam exhibiting pseudo-diode property in (a) and (c), where the enlargements of the green boxes are shown in (b) and (d).

As mentioned in Chapter 3, desired properties for application of an energy harvester include high piezo coefficient of the material, as well as low modulus for matching the resonant frequency of the environmental excitation source. Though the high piezo coefficient as well as the extreme flexibility of the doped piezo-foam make it a promising material for application of energy harvesting, the underlying mechanism of the pseudo-diode piezo-response of the doped foam needs to be further studied before drawing a conclusion as to the key factor that causes the massive piezo-response of the doped polyurethane in only one direction. The possible factors include the foaming rate, dispersion and the size of gas voids, surrounding humidity and temperature during both synthesis and polling process, polling field and polling medium (air or silicon oil), etc. However, these are not investigated further here since the aim of this thesis is to demonstrate the concept of SMSH as well as the characterization the interface circuit for large-deformation materials, instead of optimizing the flexible foam material.

Before the piezoelectric mechanism of the doped polyurethane foam is well understood and the behavior is made consistent and robust, another candidate, the THUNDER piezo-element, was studied and used in the SMSH tests in this thesis. The characterization of the THUNDER in SMSH and evaluation of the performance of the interface circuit are presented and discussed in the remainder of this chapter.

7.2 COMPARE EXPERIMENTAL AND THEORETICAL WAVEFORMS

The theory behind the improvement of output power using Synchronized-switch harvester (SSH) techniques was discussed in Chapter 3.2. In this section, the theoretical waveform of output voltage from THUNDER under the SSH is compared to the experimental

voltage waveform under the SMSH, prior to which, the comparison of theoretical and experimental output voltage under the full-wave-rectifier and resistor load are present to qualitatively verify the effectiveness of the equivalent circuit model of the THUNDER.

Figure 47 shows the tested output voltage and estimated displacement of THUNDER under a 1MOhm resistor load. The THUNDER was pressed by the shaker with a 3Hz-sinusoidal displacement represented by the dotted blue line, which is inferred by the input voltage of shaker with the assumption that phase difference between input voltage of shaker and the vibration displacement of shaker is negligible as mentioned in section 6.3.2. The result of output voltage from THUNDER (orange line) shows that the voltage profile is also sinusoidal and in-phase with the displacement at 3Hz excitation, which is the lowest frequency used to characterize the harvester in the experiment. Thus, it is reasonable to use a sinusoidal current source to model the input and output characteristic of the THUNDER under excitation of the shaker.

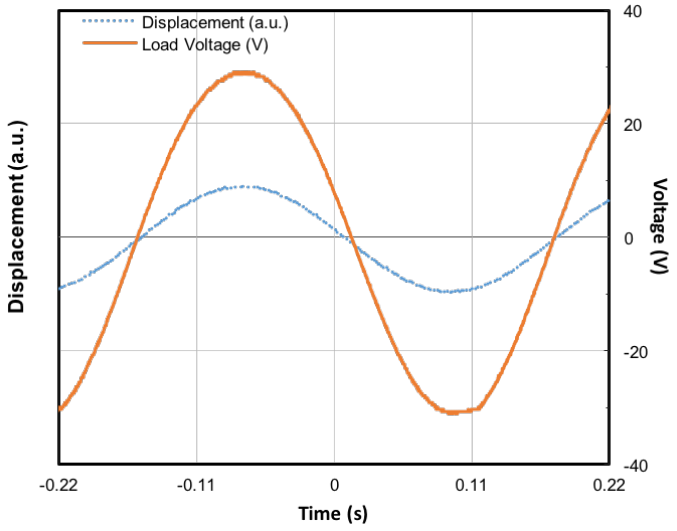

Figure 47. Experimental results of output voltage and calculated displacement of THUNDER under a 1MOhm resistor load at 3 Hz.

The comparison of theoretical and experimental output voltage of THUNDER under the Full-Wave Rectifier (FWR) is presented in Figure 48, and exhibits excellent agreement. The diagram of FWR was shown in Figure 15. The theoretical voltage performance in terms of the input current generated by the piezoelectric element was discussed in chapter 3.2. In the experimental result, the input current is calculated by shifting backward the phase of displacement by 90 degree since it is proportional to the velocity of the vibration (Hehn & Manoli 2015).

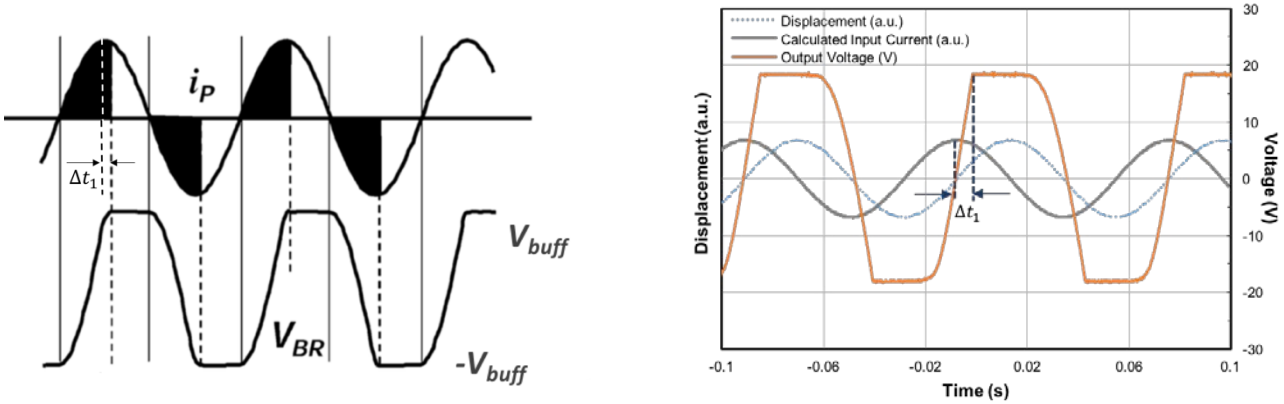

(a) **(b)**

Figure 48. (a) Theoretical and (b) experimental output voltage across THUNDER under the full-wave rectifier at 12 Hz with a buffer capacitor and 1000 kOhm resistor load.

The experimental waveforms in Figure 48(b) fit well with the prediction on the left: in a positive half-cycle of the current input, the output voltage across the THUNDER increases as the input current is charging the C_P from zero, and then levels out when it reaches the buffered load voltage V_{BUFF}. There is no current flowing to the load until the output voltage of THUNDER reaches V_{BUFF}. The shaded area of input current waveform in Figure 48(a) indicates the amount

of current that is not delivered to the load part. Notably, the output voltage is brought up to V_{BUFF} after the input current reaches its peak value, of which the time difference Δt_1 is pointed out in both Figure 48 (a) and (b). Therefore, the sum of the shaded portion in Figure 48 (a) is larger than half of a period, i.e. we can also conclude that more than a half-cycle of charge generated was not transferred to the load (or energy storage part in practical application) in FWR.

Since SMSH is replacing the electronic switch of the SSH circuit (that consists of transistors, externally powered gate circuit, and displacement sensor) with a mechanical switch, the theoretical current and voltage waveform of SSH is compared to the experimental voltage waveform of SMSH in Figure 49 to evaluate its feasibility.

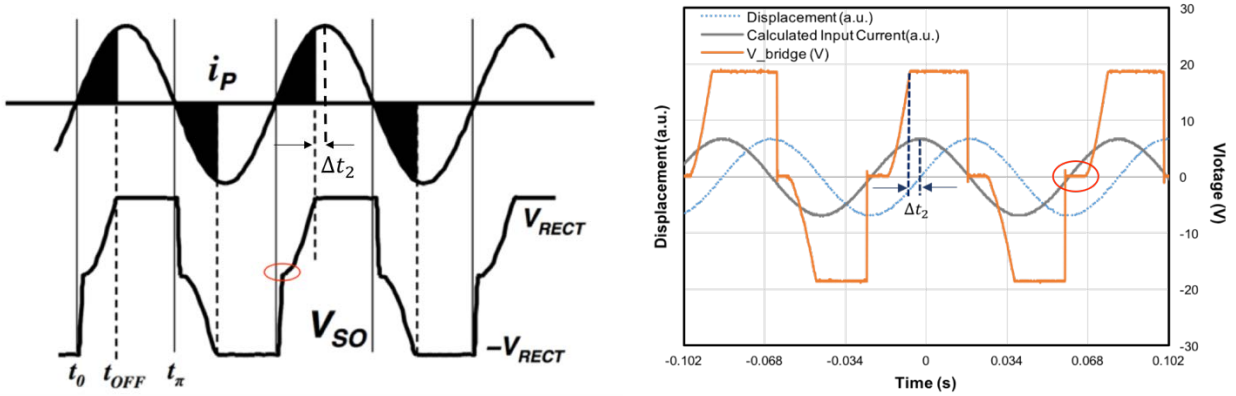

(a) **(b)**

Figure 49. (a) Theoretical voltage waveform under SSH circuit and (b) experimental output voltage across THUNDER under the SMSH circuit at 12 Hz with a buffer capacitor and 1000 kOhm resistor load

In the SMSH experimental result (in Figure 49(b)), the voltage across the THUNDER drops to zero when the switch is closed, and then rises to V_{BUFF} rapidly as soon as the switch is open. The time interval that the switch was closed is longer than that of an ideal electronic switch (See the red circles in Figure 49(a) and(b)). This is because the distance between the mechanical

switch is smaller than the vibration magnitude of THUNDER to ensure effective contact. Even though the time interval is longer, it can still be observed in this case that the output voltage reaches V_{BUFF} before the input current reach the maximum by a time of Δt_2. As a result, the generated charge that was not delivered to the load is less than a half-cycle of charge. Therefore, comparing to the wasted current of FWR, SMSH transfers more generated charge to the load.

Similarly, if the load is made up of only a resistor, the maximum voltage output (V_{max})is considerably increased compared to that of FWR as shown in Figure 50, because after each opening of the switch, the output voltage of SMSH (represented by orange line) is increased starting from 0 instead of $-V_{max}$. Therefore, comparing to the experimental waveform obtained under the full-wave rectifier, regardless of the type of load, SMSH is expected to improve the output power of the harvester in the same manner as SSH.

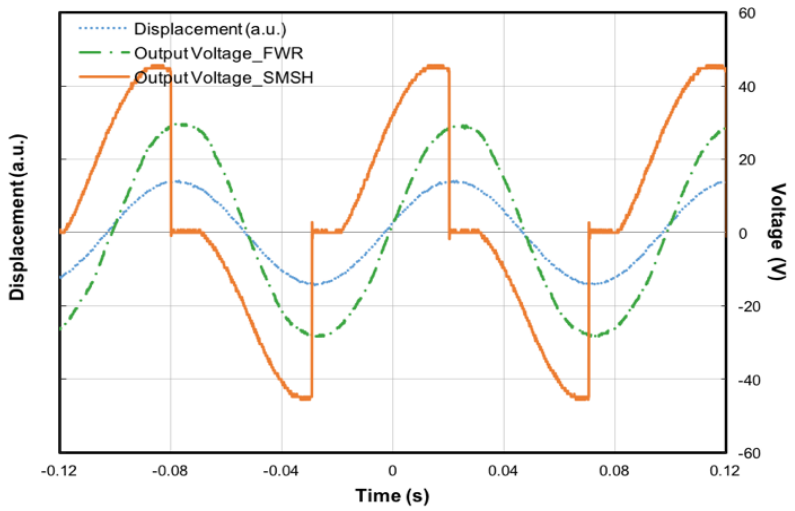

Figure 50. Experimental output voltage across THUNDER under SMSH and Full-Wave Rectifier at 10 Hz with 1000 kOhm resistor load

7.3 EXPERIMENTAL RESULT OF OUTPUT POWER FROM SMSH

7.3.1 Output power of SMSH

The output power of SMSH with pure resistor load was obtained and compared to that of a Full-Wave Rectifier circuit in terms of input frequency (See Figure 51). The output power of FWR reaches a maximum value of 2.76mW at 70 Hz, which is close to the resonant frequency of THUNDER, which is 106 Hz. Above 70Hz, the output power of FWR drops since the shaker and THUNDER system becomes non-linear. Because the displacement of THUNDER becomes opposite to the input near resonant frequency, it starts to bounce up and down between the shaker and platform and it separates from the shaker at times. A decrease of output power is thus observed even though the frequency is near resonant frequency.

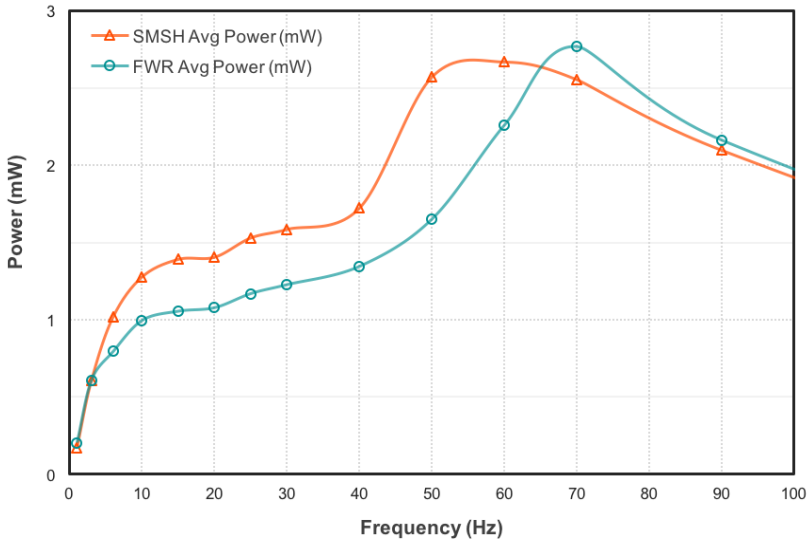

Figure 51. Comparison of output power of SMSH and FWR with 390 kOhm resistor load at different frequencies.

For the system tested, with a 390 kOhm load resistor, up to 55% increase of output power is achieved by SMSH compared to FWR in the frequency range of 4Hz to 65Hz, outside of which an equal or lower power is achieved by SMSH than FWR. The reason why less power output is achieved at less than 4 Hz as well as above 65Hz will be discussed in the next section.

7.3.2 Influential factors of output power

In order to achieve improvement of power output using the Synchronized-Switch technique, two requirements should be satisfied: (1) the switch should be closed at an appropriate time; (2) the time interval of switch closure should be as short as possible to avoid extra generated charge flowing to ground.

In the first requirement, an appropriate time for switch closure is the time when the input current crosses zero, i.e. the output voltage reaches the maximum and minimum values. However, the waveform of output voltage depends on the components of the load and is not always sinusoidal, which makes it complicated to monitor the appropriate time for switch closure. Hence, the extrema of displacement of the piezoelectric element is often measured and used to trigger the switch, with the assumption that displacement is in-phase with the output voltage of piezoelectric element. This is also the basis of SMSH where the two metallic contacts of the mechanical switch are placed at the positions of minimum and maximum displacement (See Figure 22), so that no monitor is needed.

However, the assumption of no phase shift holds only at high frequency range, where the resonant frequency of the piezo-element lies. At the low frequency range, there is phase difference between displacement and output voltage of THUNDER resulting in an inappropriate time for mechanical switch closure in the SMSH method, thus reducing the obtained power

output from SMSH in low frequency ($< 4Hz$ for the case in 7.3.1) from what could be achieved with perfect phase.

The reason why there is phase shift between the input displacement of shaker and output voltage of THUNDER, is because the capacitive piezoelectric material can form a first-order high pass filter when connecting to a load resistor (recall the equivalent circuit of harvester in Figure 13(a)), where the expressions of impedance of each component are:

$$Z_c(s) = \frac{1}{sC_p}, \quad Z_R(s) = R_L \tag{7-1}$$

Hence, the transfer function of the high pass filter is

$$H(s) \triangleq \frac{V_{out}(s)}{V_{in}(s)} = \frac{R_L}{R_L + \frac{1}{sC_p}} \tag{7-2}$$

$$|H(j\omega)| = \frac{\omega R_L C_p}{\sqrt{\left(\omega R_L C_p\right)^2 + 1}}, \qquad \angle H(j\omega) = 90° - \arctan\left(\omega R_L C_p\right) \tag{7-3}$$

Therefore, it can be known that the angle of phase shift $\angle H(j\omega)$ is related to the resistance of the load R_L, excitation frequency f, and the given piezoelectric material capacitance C_p. Only when either the R_L or f is very large can the phase difference $\angle H(j\omega)$ be ignored since the value of C_p usually lies in nF range. The measured phase shift between input voltage of shaker and the output voltage of THUNDER is shown in Figure 52.

The z axis in Figure 52 is the phase lag of output in terms of input. A negative value thus means the output is leading the input. About 90 degree of phase shift, represented by very dark blue, was found in the low frequency and low resistance region, which agrees with Equation (7-3). With the increase of frequency or resistance, the phase shift becomes close to zero. Larger

dependence on the resistance than on the frequency can be observed, which is because the measured frequency range (3 - 70Hz) is a lot lower than resistance range (0.1kΩ – 10 MΩ).

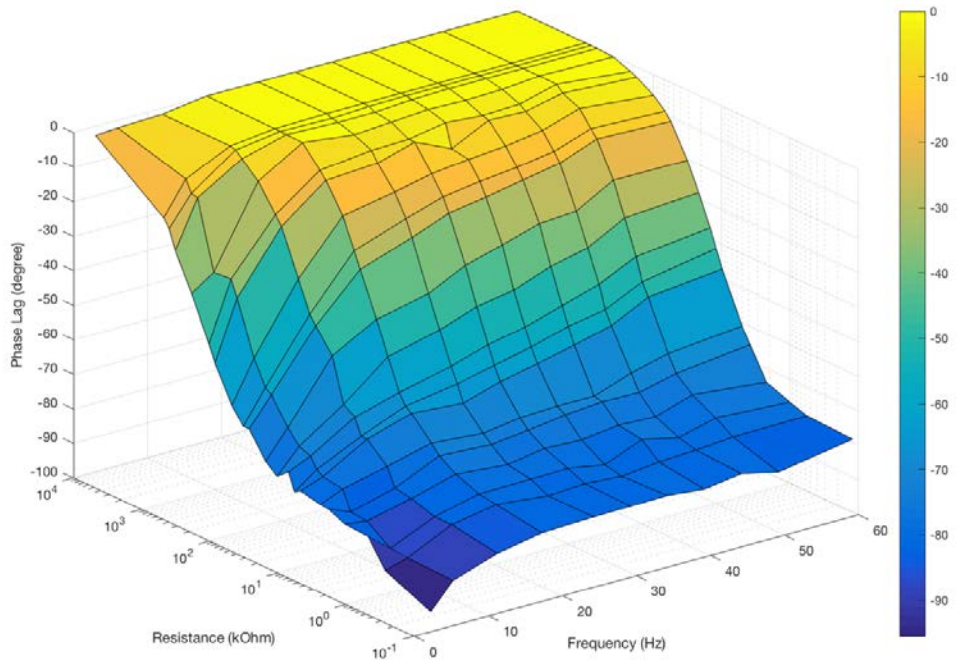

Figure 52. The dependence of load resistance and frequency of phase shift of input and output voltage

The phase shift between displacement and output voltage of THUNDER leads to a result that the switch closes at an inappropriate time. The Figure 53(a) shows that the phase of the output voltage of THUNDER connecting to FWR and 5kOhm resistor load at 10Hz leads the phase of mechanical displacement by about 80°. In this case, the maximum output voltage (V_{MAX}) and the maximum displacement (u_{MAX}) occur at staggered times. When the switch closes at u_{MAX}, the corresponding voltage is already close to 0. Thus, based on Figure 53(b), the switch is not only helpless in magnifying the voltage increase, but also reduces the output power by grounding.

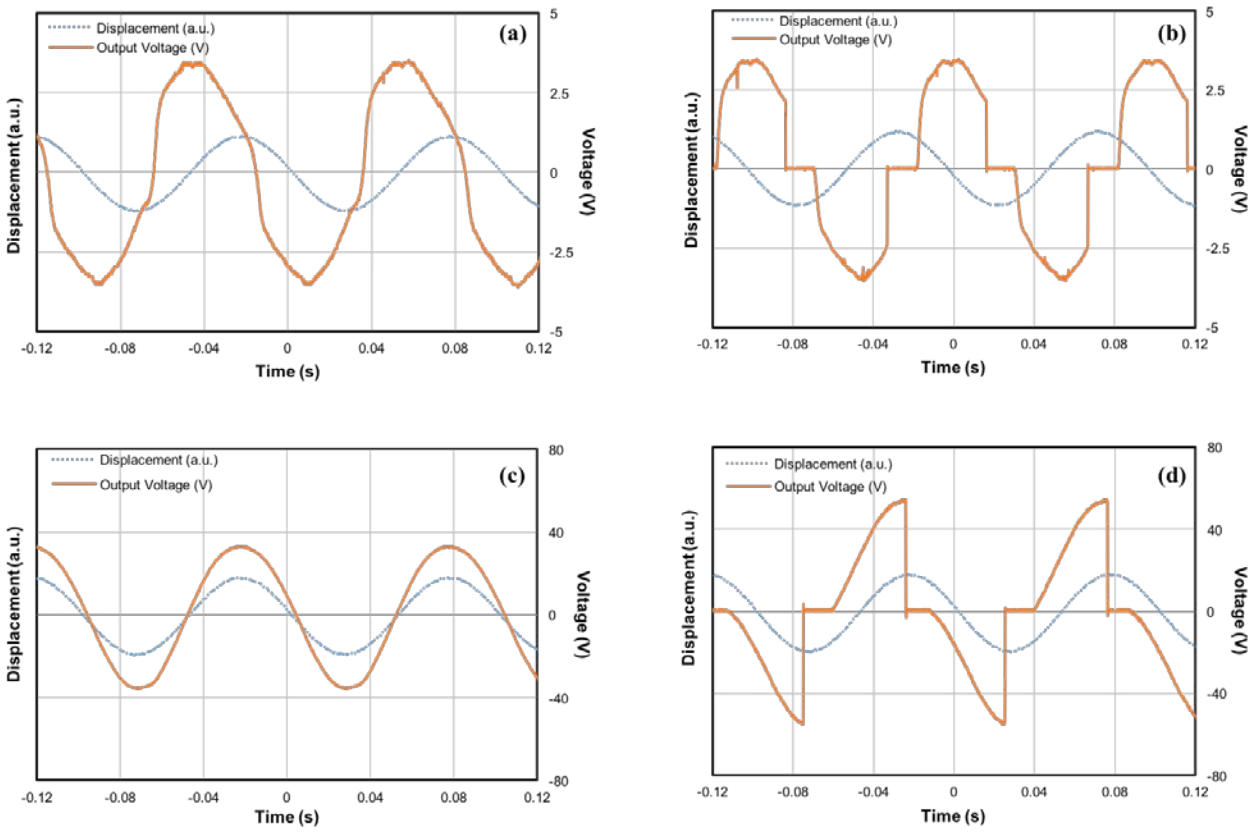

Figure 53. Output voltage and displacement waveform of THUNDER connecting to (a) FWR and (b) SMSH with 80° phase shift, and to (c) FWR and (d) SMSH with no phase shift.

If there is no phase shift, the SMSH method can achieve 63% higher V_{MAX} than that of FWR as shown in Figure 53(c) and (d), which are the waveform obtained under the condition of 10Hz and 390kOhm resistor load. Figure 54 also shows higher V_{MAX} can be obtained by SMSH with the increase of load resistance as the phase shift becomes less.

Therefore, the larger the phase shift between the input displacement and output voltage of SMSH, the less improvement of output power the SMSH can achieve. A desired region of resistance and frequency lies in the no-phase-shift region that is orange and yellow in Figure 52. Interestingly, this is just the region (off resonance) in which typical piezoelectric harvesters

perform poorly, but are also necessary regions of operation of many energy harvesting sources (e.g. repetitive, low frequency body motions).

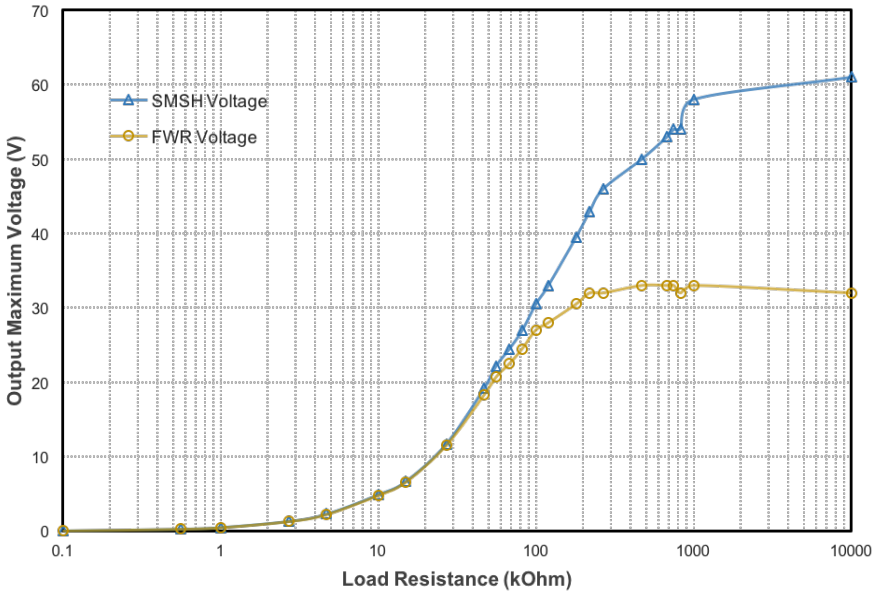

Figure 54. Comparison of maximum output voltage of SMSH and FWR connecting with different load resistance at 15Hz.

For the second requirement, the time interval over which the mechanical switch is closed (see circle annotation in Figure 49(b)), can be adjusted by changing the space between the two metallic contacts in the mechanical switch Δl as shown in Figure 55(a). It is found that the larger the space, i.e. the smaller time interval, favors higher V_{MAX}, which is shown in Figure 55(b). But after a critical value, there is little increase in V_{MAX} even with further increase in space of the switch. It should be mentioned that if the distance is too far, the mechanical switch would fail to make connection with the electrode. Thus, the distance between the two metal contacts of the

mechanical switch is set to be a bit less than the magnitude of THUNDER vibration, in order to make sure a consistent connection between the mechanical switch and the THUNDER.

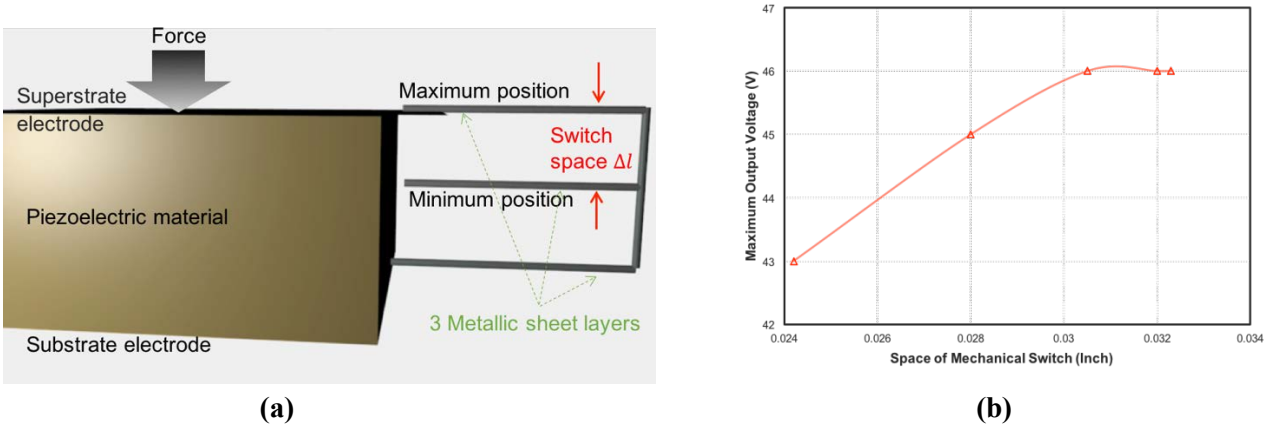

(a) **(b)**

Figure 55. (a) Schematic of SMSH structure; (b) The output voltage as a function of space of mechanical switch in SMSH with 268kOhm resistor load at 10Hz

On the other hand, a smaller time interval for switch closure is still desired for getting higher power output, even though it has less and less effect on V_{MAX}. Based on our experience, the trade-off between less time interval and stable mechanical contact of the switch often requires at least 3 milli-second of contact in SMSH. This time interval has minimal effect on both V_{MAX} and output power in the low frequency range, however, it becomes a large portion of the cycle period in the relatively high frequency range, which can severely reduce the output power by grounding the THUNDER for a large portion of a period.

For high-resistance loads, since high resistance reduces phase shift that can diminish power, the negative impact of time interval of mechanical switch closure at higher frequencies becomes the dominant factor. Figure 53(d) shows that for the output voltage waveform of SMSH under 10Hz excitation with 390kOhm resistor load, about 9ms of each closure of switch (i.e. 18%

of a period) has little effect on hindering the improvement of output power: about 28% improvement under this condition (see Figure 51).

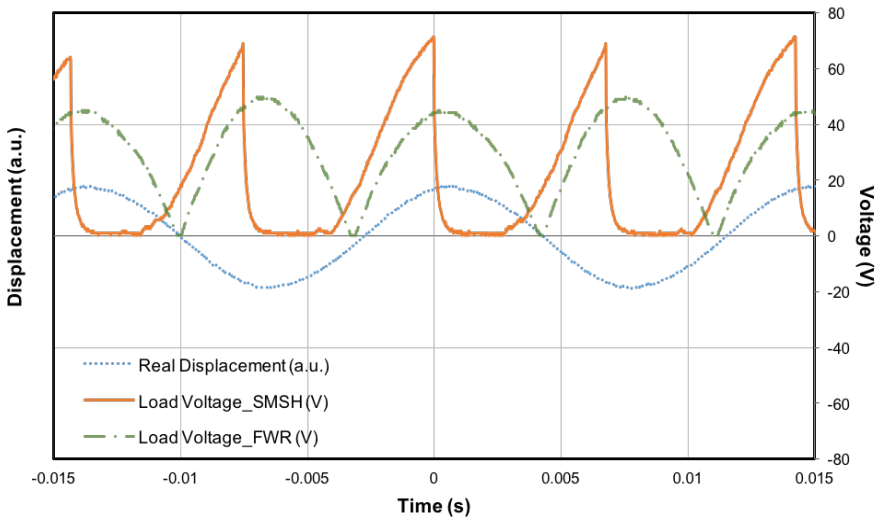

Figure 56. Load voltage waveform of SMSH and FWR with 390kOhm resistor load at 70Hz.

On the other hand, in the output voltage waveform of SMSH under 70Hz excitation shown in Figure 56, a 3ms time interval for switch closure occupies about 42% of a period. Even though the SMSH increases the V_{MAX} from 48.1 to 71.2 volts, the long grounded time that blocks energy transfer to the load significantly reduces the output power about 7%. This is the reason why less power output from SMSH than from FWR is observed above 65Hz in the case in section 7.3.1.

Therefore, with the increase of the operating frequency, the effect of phase shift is less and less, but the time interval during which the mechanical switch is closed becomes a dominant factor in determining the output power of SMSH.

7.4 CONCLUSION

To verify the feasibility of the Synchronized-Mechanical-Switch-Harvester, two candidate largely-deformed materials were investigated: CNA doped piezo-polyurethane foam and THUNDER® (thin-layer composite unimorph ferroelectric driver and sensor).

The doped piezo-foam was tested to exhibit larger piezo-response compared to commercial piezoelectric polymer PVDF with a piezocoefficient of 46pC/N. Additionally, it has an advantage of a simpler polling requirement than other piezoelectric polymers. While a pseudo-diode property was found in the doped polyurethane, a further study on the mechanism of the property and cautious control of experimental conditions for synthesis and polling of the foam are required to investigate the piezoelectricity of the material before it can be evaluated in energy harvester application.

A commercial THUNDER is thus used to evaluate the performance of the SMSH technique. Comparing to the traditional, Full-Wave Rectifier, interface circuit, up to 55% increase of output power is achieved by SMSH when connecting to the proper resistive load in the sub-resonance frequency range from 3.8% to 61% of resonant frequency. Beyond this frequency region, two factors that affect the output power of SMSH resulting in less extracted power were studied and discussed. At lower frequencies, the phase shift between input displacement of excitation and output voltage leads to an inappropriate time for the mechanical switch to close. For higher frequencies part, the time interval for during which the mechanical switch is closed occupies large portion of a period, and thereby allows less energy to be transferred to the load.

Even though these two factors may limit the operation frequency of the SMSH application, it exhibits excellent improvement of output power in the very low frequency range

where the output power of most of current piezoelectric harvesters is weak due to their high resonant frequency (kiloHertz range). Therefore, SMSH can be concluded to be a feasible and promising method flexible piezoelectric energy harvesting.

8.0 FUTURE WORK

Since this thesis is focus on evaluation of feasibility of the Synchronized-Mechanical-Switch-Harvester technique, a lot of future work can be done for optimization. Three recommendations for optimizing performance of SMSH and its implementation are suggested.

The desired range of load resistance R_L and frequency f was predicted in Figure 52 based on the phase shift between input displacement of excitation and output voltage. However, a spectrum of the R_L and f dependence of the output power of SMSH are recommended to be measured to obtain an accurate R_L and f range for optimal output power.

A displacement sensor can be employed to get more accurate deformation information of the THUNDER for investigating the relationship between mechanical input and electrical output of the energy harvester.

The structure of the mechanical switch can be optimized by using a design of adjustable mechanical switch, which can be achieved by, for instance, using a magnet so that the SMSH can exert a pulling force at various input magnitudes.

For the study of the piezoelectric foam material, the mechanism of massive piezoelectric response and the pseudo-diode property of doped piezo-foam should be further investigated by controlling experimental variables one by one.

BIBLIOGRAPHY

Aimmanee, S. & Hyer, M.W., 2004. Analysis of the manufactured shape of rectangular THUNDER-type actuators. *Smart Materials and Structures*, 13(6), pp.1389–1406.

Alemany, C. et al., 1994. Automatic iterative evaluation of complex material constants in piezoelectric ceramics. *Journal of Physics D: Applied Physics*, 27(1), p.148.

Altafi, R.A.C. et al., 2003. Piezoelectricity of multi-layers space-charge electrets from Teflon FEP film with homogeneous voids distributed on its surface. *Annual Report Conference on Electrical Insulation and Dielectric Phenomena*, (November).

Anton, S.R. & Farinholt, K.M., 2012. An evaluation on low-level vibration energy harvesting using piezoelectret foam. *Proceedings of SPIE, the International Society for Optical Engineering*, 8341.

Badel, A., 2006. Piezoelectric Energy Harvesting using a Synchronized Switch Technique. *Journal of Intelligent Material Systems and Structures*, 17(8–9), pp.831–839.

Berlincourt, D.A., Curran, D.R. & Jaffe, H., 1964. Piezoelectric and piezomagnetic materials and their function in transducers. *Physical Acoustics: Principles and Methods*, 1(Part A), p.247.

Bharti, V., Kaura, T. & Nath, R., 1995. Improved piezoelectricity in solvent-cast PVC films. *IEEE transactions on dielectrics and electrical insulation*, 2(6), pp.1106–1110.

Dargaville, T.R.T. et al., 2005. Characterization, performance and optimization of PVDF as a piezoelectric film for advanced space mirror concepts. *Optimization*, (November). Available at: http://infoserve.sandia.gov/sand_doc/2005/056846.pdf.

Fang, D. et al., 2013. Advances in Developing Electromechanically Coupled Computational Methods for Piezoelectrics/Ferroelectrics at Multiscale. *Applied Mechanics Reviews*, 65(6), pp.60802–60852. Available at: http://dx.doi.org/10.1115/1.4025633.

Flatau, A.B. et al., 2004. High-performance piezoelectric vibration energy reclamation. *SPIE*, 5390, p.379.

Fu, J., Hou, Y., Wei, Q., et al., 2015. Advanced FeTiNbO6 / poly (vinylidene fluoride) composites with a high dielectric permittivity near the percolation threshold. *Journal of Applied Physics*, 235502, p.118. Available at: http://dx.doi.org/10.1063/1.4937581.

Fu, J., Hou, Y., Zheng, M., et al., 2015. Improving Dielectric Properties of PVDF Composites by Employing Surface Modified Strong Polarized BaTiO3 Particles Derived by Molten Salt Method. *ACS Applied Materials Interfaces*, 7, pp.24480–24491.

Guyomar, D. et al., 2005. Toward energy harvesting using active materials and conversion improvement by nonlinear processing. *IEEE transactions on ultrasonics, ferroelectrics, and frequency control*, 52(4), pp.584–595.

Guyomar, D., Richard, T. & Richard, C., 2007. Sound Wave Transmission Reduction through a Plate using Piezoelectric Synchronized Switch Damping Technique. *Journal of Intelligent Material Systems and Structures*, 19(7), pp.791–803.

Harrison, J.S. & Ounaies, Z., 2001. Piezoelectric Polymers. *Encyclopedia of Polymer Science and Technology*, 3. Available at: http://scholar.google.com/scholar?q=Piezoelectric Polymers Harrison&ie=UTF-8&oe=utf-8&rls=org.mozilla:en-US:official&client=firefox-a&um=1&sa=N&tab=ws%5Cnhttp://dx.doi.org/10.1002/0471440264.pst427.

Haun, M.J., 1983. *Transverse Reinforcement of 1-3 and 1-3-0 PZT-Polymer Piezoelectric Composites with Glass Fibers*. Pennsylvania State University.

Hehn, T. & Manoli, Y., 2015. *CMOS Circuits for Piezoelectric Energy Harvesters*, Springer Dordrecht Heidelberg New York London.

HILCZER, B. & MALECKI, J., 1986. Electrets: Studies in Electrical and Electronic Engineering. *Elsevier*, 14.

Hillenbrand, J. et al., 2002. Piezoelectricity of cellular and porous polymer electrets. In *International symposium on electrets*.

Hillenbrand, J. & Sessler, G.M., 2004. Quasistatic and Dynamic Piezoelectric Coefficients of Polymer Foams and Polymer Film Systems. *IEEE Transactions on Dielectrics and Electrical Insulation*, 11(1), pp.72–79.

Hongduo, Z., Jian, Y. & Jianming, L., 2010. Finite element analysis of Cymbal piezoelectric transducers for harvesting energy from asphalt pavement. *Journal of the Ceramic Society of Japan*, 118(1382), pp.909–915.

Jaffe, B., Roth, R.S. & Marzullo, S., 1954. Piezoelectric properties of Lead zirconate-Lead titanate solid-solution ceramics [8]. *Journal of Applied Physics*, 25(6), pp.809–810.

Jin, L., Li, F. & Zhang, S., 2014. Decoding the fingerprint of ferroelectric loops: Comprehension of the material properties and structures. *Journal of the American Ceramic Society*, 97(1), pp.1–27.

Kawai, H., 1970. Electrostriction and piezoelectricity of elongated polymers films. *Oyo Buturi*, 39, pp.413–419.

Khan, F. & Ahmad, I., 2016. Review of Energy Harvesters Utilizing Bridge Vibrations. *Shock and Vibration*, 2(1), p.21.

Kim, H.W. et al., 2005. Piezoelectric energy harvesting under high pre-stressed cyclic vibrations. *Journal of Electroceramics*, 15(1), pp.27–34.

Kim, J.Y.-H., Cheng, A. & Tai, Y.-C., 2011. Parylene-C as a piezoelectric material. In *IEEE Micro Electro Mechanical Systems (MEMS)*.

Kim, S.-G., Priya, S. & Kanno, I., 2012. Piezoelectric MEMS for energy harvesting. *MRS Bulletin*, 37(11), pp.1039–1050.

Kim, Y. et al., 2009. Fabrication and characterization of THUNDER actuators—pre-stress-induced nonlinearity in the actuation response. *Smart Materials and Structures*, 18(9), p.95033.

Kong, N.A. et al., 2010. Resistive impedance matching circuit for piezoelectric energy harvesting. *Journal of Intelligent Material Systems and Structures*, 21(13), pp.1293–1302.

Lee, M.-H., Halliyal, A. & Newnham, R.E., 1988. Poling studies of piezoelectric composites prepared by coprecipitated PbTiO3 powder. *Ferroelectrics*, 87(1), pp.71–80.

Lee, Y.H. et al., 1986. Preparation of PbTiO 3 powder for a flexible 0-3 piezoelectric composite. In *Applications of Ferroelectrics. 1986 Sixth IEEE International Symposium on*. IEEE, pp. 318–322.

Lefeuvre, E., 2006. Semi-passive Piezoelectric Structural Damping by Synchronized Switching on Voltage Sources. *Journal of Intelligent Material Systems and Structures*, 17(8–9), pp.653–660.

Li, C. et al., 2008. Flexible Dome and Bump Shape Piezoelectric Tactile Sensors Using PVDF-TrFE Copolymer. *Journal of Microelectromechanical Systems*, 17(2), pp.334–341.

Li, H., Tian, C. & Deng, Z.D., 2014. Energy harvesting from low frequency applications using piezoelectric materials. *Applied Physics Reviews*, 1(4).

Ma, H. et al., 2002. Highly Efficient and Thermally Stable Electro-Optical Dendrimers for Photonics. *Advanced Functional Materials*, 12(9), pp.565–574.

McSkimin, H.J. & Andreatch Jr, P., 1967. Measurement of very small changes in the velocity of ultrasonic waves in solids. *The Journal of the Acoustical Society of America*, 41(4B), pp.1052–1057.

Mitcheson, P.D. et al., 2004. Architectures for vibration-driven micropower generators. *Journal of microelectromechanical systems*, 13(3), pp.429–440.

Moody, M.J., Marvin, C.W. & Hutchison, G.R., 2016. Molecularly-doped polyurethane foams with massive piezoelectric response. *J. Mater. Chem. C*, 4(20), pp.4387–4392.

Mopsik, F.I. & Broadhurst, M.G., 1975. Molecular dipole electrets. *Journal of Applied Physics*, 46(10), pp.4204–4208.

Moulson, A.J. & Herbert, J.M., 1990. Materials, Properties, Applications. In *Electroceramics*. London, UK: Chapman and Hall, pp. 265–317.

Newman, B.A. et al., 1980. Piezoelectricity in nylon 11. *Journal of Applied Physics*, 51(10), pp.5161–5164.

Nye, J.F., 1985. *Physical properties of crystals: their representation by tensors and matrices*, Oxford university press.

Owczarek, M. et al., 2016. Flexible ferroelectric organic crystals. *Nature Communications*, 7, p.13108. Available at: http://www.nature.com/doifinder/10.1038/ncomms13108.

Polla, D.L. & Francis, L.F., 1998. Processing and characterization of piezoelectric materials and integration into microelectromechanical systems. *Annual review of materials science*, 28(1), pp.563–597.

Popovici, D., Akedo, J. & Okuyama, M., 2011. *Barium Titanate-Based Materials-a Window of Application Opportunities*, INTECH Open Access Publisher.

Ramadan, K.S., Sameoto, D. & Evoy, S., 2014. A review of piezoelectric polymers as functional materials for electromechanical transducers. *Smart Materials and Structures*, 23(3), p.33001.

Ramadass, Y.K., 2009. *Energy Processing Circuits for Low-Power Applications*. MASSACHUSETTS INSTITUTE OF TECHNOLOGY.

Renaud, M. et al., 2008. Fabrication, modelling and characterization of MEMS piezoelectric vibration harvesters. *Sensors and Actuators A: Physical*, 145, pp.380–386.

Renaud, M. et al., 2007. Piezoelectric harvesters and MEMS technology: fabrication, modeling and measurements. In *Solid-State Sensors, Actuators and Microsystems Conference, 2007. TRANSDUCERS 2007. International*. IEEE, pp. 891–894.

Rosen, C.Z., Hiremath, B. V & Newnham, R., 1992. IEEE standard on piezoelectricity (ANSI/IEEE Standard 176-1987 1988). *Key Papers in Physics*.

Roundy, S., Wright, P.K. & Rabaey, J., 2003. A study of low level vibrations as a power source for wireless sensor nodes. *Computer communications*, 26(11), pp.1131–1144.

Ryu, J. et al., 2001. Magnetoelectric properties in piezoelectric and magnetostrictive laminate composites. *Japanese Journal of Applied Physics*, 40(8R), p.4948.

Shen, H., Qiu, J. & Balsi, M., 2011. Vibration damping as a result of piezoelectric energy harvesting. *Sensors and Actuators A: Physical*, 169(1), pp.178–186.

Shenck, N.S. & Paradiso, J.A., 2001. Energy scavenging with shoe-mounted piezoelectrics. *IEEE micro*, 21(3), pp.30–42.

Sherrit, S. & Mukherjee, B.K., 2007. Characterization of Piezoelectric Materials for Transducers. *Arxiv preprint arXiv*, 7112657.

Shi, Y. et al., 2000. Low (sub-1-volt) halfwave voltage polymeric electro-optic modulators achieved by controlling chromophore shape. *Science*, 288(5463), pp.119–122.

Shu, Y.C. & Lien, I.C., 2006. Analysis of power output for piezoelectric energy harvesting systems. *Smart materials and structures*, 15(6), p.1499.

Stefanou, H., 1979. The application of a dipolar theory to the piezoelectricity in vinylidene fluoride–co-tetrafluoroethylene polymers. *Journal of Applied Physics*, 50(3), pp.1486–1490. Available at: http://dx.doi.org/10.1063/1.326134.

Takahashi, Y., Iijima, M. & Fukada, E., 1989. Pyroelectricity in poled thin films of aromatic polyurea prepared by vapor deposition polymerization. *Japanese journal of applied physics*, 28(12A), p.L2245.

Tashiro, K., 1995. Crystal structure and phase transition of PVDF and related copolymers. In H. Singh Nalwa, ed. *Ferroelectric Polymers*. New York, pp. 63–180.

TE_Sensor_Solutions, 2015. DT Series Elements. *datasheet*, (757), p.8008.

Tichý, J. et al., 2010. *Fundamentals of Piezoelectric Sensorics*, Springer.

Turner, R.C. et al., 1994. Materials for high temperature acoustic and vibration sensors: A review. *Applied acoustics*, 41(4), pp.299–324.

Wang, H., Zhang, Q. & Cross, L.E., 1993. A high sensitivity, phase sensitive d33 meter for complex piezoelectric constant measurement. *Japanese journal of applied physics*, 32(9A), p.L1281.

Williams, C.B. & Yates, R.B., 1996. Analysis of a micro-electric generator for microsystems. *Sensors and Actuators A: Physical*, 52(1–3), pp.8–11.

Windmill, J.F.C. et al., 2008. Nanomechanical and electrical characterization of a new cellular electret sensor-actuator. *Nanotechnology*, 19.

Wise, E. et al., 2002. In Situ Poling and Imidization Piezoelectric Polyimides of Amorphous.

Yu, L. & Cebe, P., 2009. Effect of nanoclay on relaxation of poly(vinylidene fluoride) nanocomposites. *Journal of Polymer Science, Part B: Polymer Physics*, 47(24), pp.2520–2532.